A GluN2B mutation identified in Autism prevents NMDA receptor trafficking and interferes with dendrite growth

†Michael P. Sceniak[1], †Karlie N. Fedder[2], Qian Wang[1], Sammy Droubi[2], Katie Babcock [1], Sagar Patwardhan[2], Jazmin Wright-Zornes[1], Lucynda Pham[1] and Shasta L. Sabo[1,2,*]

[1]Department of Biology, Central Michigan University

[2]Departments of Pharmacology and Neuroscience, Case Western Reserve University School of Medicine

†Authors contributed equally

*corresponding author: sabo1s@cmich.edu

Summary statement:

GRIN2B mutations cause ASD, but the pathogenic mechanisms remain unknown. Our data suggest that ASD-specific *GRIN2B* mutations interfere with NMDA receptor trafficking and lead to reduced dendrite elongation and branching.

JCS Advance Online Article. Posted on 23 September 2019

Abstract:

Autism spectrum disorders (ASD) are neurodevelopmental disorders with multiple genetic associations. Analysis of *de novo* mutations identified *GRIN2B*, which encodes the GluN2B subunit of NMDA receptors, as a high-probability ASD gene. However, the mechanisms by which *GRIN2B* mutations contribute to ASD pathophysiology are not understood. Here, we investigated the cellular phenotypes induced by a human mutation that is predicted to truncate GluN2B within the extracellular loop. This mutation abolished NMDA-dependent calcium influx. Mutant GluN2B co-assembled with GluN1 but was not trafficked to the cell surface or dendrites. When mutant GluN2B was expressed in developing cortical neurons, dendrites appeared underdeveloped, with shorter and fewer branches, while spine density was unaffected. Mutant dendritic arbors were often dysmorphic, displaying abnormal filopodial-like structures. Interestingly, dendrite maldevelopment appeared when mutant GluN2B was expressed on a wild-type background, reflecting the disease as individuals are heterozygous for *GRIN2B* mutations. Restoring the fourth transmembrane domain and cytoplasmic tail did not rescue the phenotypes. Finally, abnormal development was not accompanied by reduced mTOR signaling. These data suggest that mutations in *GRIN2B/*GluN2B contribute to ASD pathogenesis by disrupting dendrite development.

Introduction:

Autism Spectrum Disorders (ASD) are a family of complex neurodevelopmental disorders characterized by restricted, repetitive behaviors and interests, impaired social interactions and difficulty with communication. ASD is highly heritable, and *de novo* protein-altering mutations are thought to cause a high percentage of ASD cases (Krumm et al., 2014). *De novo* mutations in the *GRIN2B* gene, which encodes the GluN2B subunit of NMDA receptors (NMDARs), have been identified in multiple probands with sporadic ASD but not in unaffected siblings or other control individuals (De Rubeis et al., 2014; Iossifov et al., 2014; Kenny et al., 2014; Myers et al., 2011; O'Roak et al., 2011; O'Roak et al., 2012b; O'Roak et al., 2014; Pan et al., 2015; Platzer et al., 2017; Sanders et al., 2015; Takasaki et al., 2016; Talkowski et al., 2012; Tarabeux et al., 2011; Yoo et al., 2012). The recurrence of *de novo* ASD-associated mutations in *GRIN2B* and rigorous analyses indicate that *GRIN2B* is a true ASD gene (De Rubeis et al., 2014; Iossifov et al., 2014; O'Roak et al., 2012b; Stessman et al., 2017). However, we are only beginning to understand the impact of ASD-associated *GRIN2B* mutations on NMDAR function (Fedele et al., 2018; Liu et al., 2017; Vyklicky et al., 2018), and it is not yet clear how *GRIN2B* mutations alter neuronal development to cause ASD.

NMDARs are ionotropic glutamate receptors that are important for neuronal development and plasticity (Sanz-Clemente et al., 2013). These receptors are tetramers comprised of two GluN1 subunits and two GluN2 and/or GluN3 subunits. Within the assembled receptor, GluN2 subunits are necessary for glutamate-dependent activation and subcellular trafficking (Horak et al., 2014). While GluN2B-containing receptors can be found in the axon and presynaptic terminals in developing cortex and hippocampus (Berg et al., 2013; Charton et al., 1999; DeBiasi et al., 1996; Gill et al., 2015; Jourdain et al., 2007; Larsen et al.; Larsen et al., 2014; McGuinness et al., 2010), most GluN2B-containing receptors are found within dendrites.

GluN2B is essential for normal development. During postnatal development, most NMDARs in the cortex and hippocampus contain GluN2B (Komuro and Rakic, 1993; Monyer et al., 1994; Watanabe et al., 1992). GluN2B homozygous knockout mice die around birth (Kutsuwada et al., 1996), and genetic substitution of GluN2A for GluN2B does not rescue this lethality (Hamada et al., 2014; Wang et al., 2011). Moreover, genetically replacing GluN2B with GluN2A results in reduced social exploration in surviving mice, even when total NMDAR currents are equivalent (Wang et al., 2011). In addition, abnormal expression or function of GluN2B-containing NMDARs

has been observed in mouse models of ASD and ASD-related neurodevelopmental disorders, including Rett syndrome, Fragile X syndrome and fetal valproate exposure (for examples, see: (Asaka et al., 2006; Bostrom et al., 2015; De Filippis et al., 2015; Etherton et al., 2011; Krueger et al.; Lee et al., 2008; Mierau et al., 2016; Roullet et al., 2010; Sceniak et al., 2016; Schutt et al., 2009; Stefanovic et al., 2015; Toft et al., 2016; Wang et al., 2018).

Symptoms and diagnosis of ASD frequently occur by the age of 3 (Bourgeron, 2009). This timing suggests that aspects of neuronal development that occur during this period underlie autism pathogenesis. Several studies have demonstrated roles for GluN2B in regulation of dendrite growth and patterning (Bustos et al., 2014; Espinosa et al., 2009; Ewald et al., 2008; Keith et al., 2019; Sepulveda et al., 2010), and abnormal dendrite architecture is often associated with ASD (Gao and Penzes, 2015; Lin et al., 2016; Varghese et al., 2017). Therefore, we hypothesized that ASD-associated mutations in GluN2B dysregulate elaboration of dendritic arbors.

To begin to understand how mutations in GluN2B contribute to ASD pathogenesis, we focused on a *de novo* single nucleotide variant mutation in *GRIN2B* that was identified in a patient with severe, early onset simplex ASD (O'Roak et al., 2011). This human mutation is predicted to produce a premature stop within the second extracellular loop of GluN2B, but the biological effects of this mutation have not yet been studied. Here, we evaluated the impact of this ASD-associated mutation in GluN2B on NMDAR function, receptor trafficking and cortical excitatory neuron development. We find that mutant receptors are completely non-functional and are trafficked neither to the cell surface nor into dendritic spines. Expression of ASD mutant GluN2B subunits led to dramatic defects in dendrite growth and branching. Dendrite maldevelopment occurred when mutant GluN2B was expressed in the presence of wild-type GluN2B. Importantly, this parallels the disease since ASD patients have mutation of only one allele of the gene. While dendritic arbors were smaller, dendritic spine density was unchanged, suggesting that total synapse number was reduced. Together, these data suggest that ASD mutations that severely disrupt NMDA receptor trafficking and function may contribute to ASD pathophysiology by limiting dendrite development, thereby disrupting normal circuit function.

Results:

ASD mutant GluN2B abolishes channel activity

To investigate the cellular and molecular phenotypes resulting from patient *GRIN2B* mutations, we investigated a *GRIN2B* variant that was identified in a female proband (SSC proband # 12681) who was clinically diagnosed with ASD and met the Autism Diagnostic Observation Schedule research criteria for ASD (O'Roak et al., 2011). As described by O'Roak and colleagues (2011), this proband's symptoms were severe, with a Calibrated Severity Score of 9 (with 10 corresponding to the most severe score possible). She showed impaired overall adaptive behaviors (6^{th} percentile). Her communication abilities were ranked at the 5^{th} percentile, and social-emotional behaviors at the 18^{th} percentile. The proband exhibited comorbid intellectual disability, with a full-scale IQ of 63 and a non-verbal IQ of 65, both at the 1^{st} percentile. The affected individual used language fluently, but did display language delay. Onset of ASD was early, prior to age 3, with possible regression. The proband had unaffected parents, each with no psychiatric history, and two siblings who were both unaffected. Importantly, this mutation has not been found in any unaffected individuals (O'Roak et al., 2011; O'Roak et al., 2012a; O'Roak et al., 2012b; O'Roak et al., 2014).

The single-nucleotide mutation identified in this proband (12681) was initially described by O'Roak et al. (2011) and expected to be a loss of function mutation (O'Roak et al., 2011; O'Roak et al., 2012a; O'Roak et al., 2012b). This variant (c.2172-2A>G) is predicted to be protein truncating (O'Roak et al., 2012a). Therefore, we modeled the mutation in GluN2B cDNA by introducing a stop codon within the second extracellular loop after amino acid 724 (**Fig. 1A**), corresponding to the end of exon 10 of *GRIN2B* and the predicted truncation site. This construct is referred to here as $GluN2B^{724t}$.

Because it seemed possible that the conformational changes caused by the truncation could alter the affinity of anti-GluN2B antibodies for the mutant protein, we produced the mutation in GluN2B with a GFP tag inserted in the amino terminal domain, after the signal peptide, to allow reliable visualization of the mutant GluN2B. It is well-established that the template GFP-GluN2B construct expresses well, functions normally, and traffics properly (Luo et al., 2002). When HEK-

293 cells were transfected with GFP-GluN2B^{724t} or GFP-GluN2B^{WT} (wild-type), expression levels and transfection efficiencies for the two proteins appeared similar (**Fig. 1B**).

To determine whether this GluN2B mutation alters NMDA receptor function, we transfected HEK-293 cells with cDNAs encoding either wild type GluN2B (GluN2B^{WT}) or the GluN2B^{724t} mutant, along with GluN1-1a tagged with HcRed. Heterologous expression avoids the complications of endogenous wild-type GluN2B expressed in neurons. At 24-48h after transfection, we used Fluo4 to image calcium influx in response to brief perfusion with NMDA (100uM) in the presence of glycine (10uM) and absence of magnesium. Wild-type NMDA receptors consistently produced a profound NMDA-dependent increase in intracellular calcium (**Fig. 1B-D,** n = 80 cells from 4 independent experiments, maximal $\Delta F/F_o$ (fold change in fluorescence, normalized to baseline): 0.796 +/- 0.009). In stark contrast, NMDA failed to induce a calcium response in all cells transfected with GluN2B^{724t} (**Fig. 1B-D,** n = 40 cells from 4 independent experiments, maximal $\Delta F/F_o$: -0.012+/- 0.002, p = 1.36 X 10^{-10}). In all cases, NMDA-dependent calcium influx was completely blocked in the same cells upon exposure to an NMDA receptor antagonist, ketamine (**Fig. 1B-C**). These data suggest that GluN2B^{724t} is unable to form functional receptors.

ASD associated GluN2B mutations prevent surface expression of NMDARs

GluN2B subunits have a well-established role in controlling the subcellular trafficking of NMDARs (Horak et al., 2014). Therefore, the observed impairments in receptor function could be due to disrupted subcellular trafficking. To test this hypothesis, we selectively labeled GluN2B at the cell surface in HEK-293 cells co-transfected with GluN1 and either GFP-GluN2B or GFP-GluN2B^{724t} (**Fig. 2**). To selectively visualize surface receptors, we labeled living, non-permeabilized cells with antibodies against the GFP tag, which was localized to the amino terminal extracellular domain of GluN2B. Then, labeled cells were fixed and observed by confocal microscopy. No surface labeling was detected without GluN2B transfection or when antibodies to intracellular epitopes were used. In addition, no labeling was observed when cells were transfected with cytosolic GFP instead.

Surface expression of GluN2B was markedly different between GluN2B^{724t} and GluN2B^{WT} (**Fig. 2**). As expected, GluN2B^{WT} was abundant at the cell surface (**Fig. 2A-B**). Strikingly, GluN2B^{724t} was nearly absent from the cell surface (**Fig. 2A-B**). GluN2B^{724t} expressing cells

showed minimal surface expression (surface fluorescence normalized to wild-type surface fluorescence: 0.29 +/- 0.03 (GluN2B^{724t}), n = 41 cells; p < 0.0001) when compared to cells transfected with GluN2B^{WT} (1.00 +/- 0.12, n = 64 cells). Similar results were observed using two distinct anti-GFP antibodies. The observed change in surface expression was not a result of reduced overall expression of GluN2B since total expression levels of GFP-GluN2B^{WT} and GFP-GluN2B^{724t} were not significantly different (**Fig 2C**, total GluN2B expression, normalized to wild-type: 1.00 +/- 0.16 (GluN2B^{WT}), 0.71 +/- 0.15 (GluN2B^{724t}); p = 0.215). Next, we measured the total expression of GluN1 in order to confirm that differences in GluN2B expression at the cell surface reflected the effects of the mutation rather than differences in co-transfection efficiency or GluN1 expression levels. As shown in **Fig. 2D**, GluN1 expression levels were not significantly different in wild-type and mutant cells (total GluN1 fluorescence, normalized to wild-type: 1.00 +/- 0.09 (GluN2B^{WT}, n = 16 cells), 1.17 +/- 0.12 (GluN2B^{724t}, n = 17 cells); p = 0.2291). These data indicate that the GluN2B^{724t} ASD-associated mutation prevents trafficking of NMDARs to the cell surface.

The last transmembrane domain and the carboxy-terminal cytoplasmic tail of GluN2B both play a role in trafficking of GluN2B to the cell surface (Chung et al., 2004; Hawkins et al., 2004; Horak et al., 2008; Mori et al., 1998; Prybylowski et al., 2005; Sans et al., 2003; Steigerwald et al., 2000), and both are missing in the GluN2B^{724t} mutant. Therefore, we wondered whether the defects in GluN2B trafficking could be rescued by restoring the 4th transmembrane domain and cytoplasmic tail. To test this, we created a mutant that still lacked a significant portion of the deleted sequence in the extracellular loop but maintained the transmembrane domain and cytoplasmic tail. Interestingly, this deletion mutant, GluN2B$^{\Delta 724\text{-}786}$, was not trafficked to the cell surface (**Fig. 2E-F;** surface fluorescence normalized to wild-type: GluN2B$^{\Delta 724\text{-}786}$: 0.27 +/- 0.04, n = 60 cells; wild-type: 1.0 +/- 0.12, n = 55 cells, p < 0.0001), phenocopying the truncation mutant. Therefore, loss of a portion of the extracellular loop is sufficient to disrupt GluN2B trafficking.

The lack of trafficking of GluN2B to the cell surface could be a result of impaired co-assembly with the obligatory subunit, GluN1. Therefore, we next asked whether GluN2B^{724t} interacts with GluN1. To test this, lysates of HEK cells transfected with GluN1 and either GFP-GluN2B^{724t} or GFP-GluN2B^{WT} were subjected to immunoprecipitation with anti-GFP antibodies followed by immunoblotting for GluN1 and GluN2B (**Fig 2G**). GluN1 co-precipitated with both wild-type and mutant GluN2B, suggesting that GluN2B^{724t} can co-assemble with GluN1.

ASD mutant GluN2B is missorted within neurons

Since the mutation prevented trafficking of GluN2B to the cell surface in HEK-293 cells, we next asked whether GluN2B^{724t} receptors are trafficked appropriately within neurons. To do so, we transfected wild-type rat cortical neurons with GFP-GluN2B^{WT} or GFP-GluN2B^{724t}. When the localization of GluN2B was examined in developing excitatory neurons, GluN2B^{WT} puncta were distributed throughout the dendritic arbor; however, GluN2B^{724t} failed to localize to dendritic puncta (**Fig. 3A**). Instead, GluN2B^{724t} was restricted to the soma and occasional proximal dendrites. In some cases, faint GFP-GluN2B^{724t} signal was observed a bit farther into the dendritic tree, but in these cases the signal was diffuse rather than punctate. Within dendrites, GFP-GluN2B^{WT} puncta were often associated with dendritic spines, whereas mutant GFP-GluN2B puncta were not observed in spines (**Fig. 3B**).

The mutation also prevented trafficking to the surface of neurons. When neurons were transfected with either with GFP-GluN2B^{WT} or GFP-GluN2B^{724t} followed by live labeling with anti-GFP antibodies, GluN2B^{WT} was observed in discrete puncta at the surface of dendrites, as expected (**Fig. 4A**). In contrast, GluN2B^{724t} was not observed at the cell surface (**Fig. 4A**). Quantification of surface GFP-GluN2B verified that the mutation prevented trafficking of GluN2B to the cell surface (**Fig. 4B;** surface GluN2B fluorescence, normalized to wild-type: 1.00 +/- 0.20 (GluN2B^{WT}), 0.11 +/- 0.05 (GluN2B^{724t}); $p = 2.95 \times 10^{-4}$; n = 13 GluN2B^{724t} and 14 GluN2B^{WT} neurons). The lack of GluN2B^{724t} trafficking to dendrites and the neuronal cell surface was not due to reduced expression of the mutant protein since neurons chosen for analysis expressed GFP at similar moderate levels (**Fig. 4C;** total GluN2B, normalized to wild-type: 1.00 +/- 0.07 (GluN2B^{WT}), 1.18 +/- 0.22 (GluN2B^{724t}); p = 0.4397).

GluN2B^{724t} expression interferes with dendrite branching and extension

The experiments above were performed in wild-type neurons expressing endogenous wild-type GluN1 and GluN2B. Unexpectedly, wild-type neurons that expressed the GluN2B^{724t} mutant had profoundly abnormal dendritic architectures (**Fig. 5A**). In contrast, neurons expressing GFP-GluN2B^{WT} had normal dendritic arbors (**Fig. 5A**). Two types of abnormal dendrite growth were observed when mutant GluN2B was present. In some mutant neurons, the dendrites appeared to be underdeveloped, with shorter and fewer branches than wild-type neurons (**Fig. 5A-B**). In other mutant neurons, dendrites were highly dysmorphic, often

appearing as a mass of hairy extensions or lamellipodia-like structures protruding from the soma rather than *bona fide* branches. Neurons expressing GluN2B^{WT} almost always appeared normal and never appeared dysmorphic (**Fig. 5B,** 83.33% normal, 8.33 % underdeveloped, 0% dysmorphic, n = 12 neurons). Strikingly, neurons expressing GluN2B^{724t} rarely appeared normal (**Fig. 5B;** 6.25% normal, 43.75% underdeveloped, 31.25% dysmorphic, n = 16 neurons). The abnormal structures of dysmorphic neurons typically lacked the dendrite marker MAP2 (**Fig. S1**), although MAP2 could be seen at the bases of some structures. MAP2 was observed in structures that otherwise appeared to be short dendrites that were thicker and longer than normal filopodia. Importantly, the observed effects of the GluN2B mutation on dendrite growth were cell-autonomous since neurons were sparsely transfected, so each transfected neuron was surrounded by untransfected neurons.

To quantify the effects of GluN2B^{724t} on dendrite extension and branching, we performed Sholl analysis. In Sholl plots, there was a clear distinction between the dendritic architecture of neurons expressing GFP-GluN2B^{WT} and those expressing GFP-GluN2B^{724t} (**Fig. 5C**). While the number of branches close to the soma appeared to be similar, expression of mutant GluN2B dramatically reduced the number of branches found farther from the soma. Abnormal dendrite morphology could result from changes in the number of dendrite branches, the length of dendrite segments, or both. To distinguish between these possibilities, we quantified these measures in several ways. GluN2B^{724t} mutant neurons had significantly fewer overall branches (**Fig. 5D,** 29.17 +/- 2.01 (wt) and 24.07 +/- 1.51 (724t) branch points per neuron; $p = 0.005$, n = 12 (WT) and 15 (724t) neurons) and fewer terminal branches (**Fig. 5E,** 36.0 +/- 1.87 (wt) and 30.06 +/- 1.67 (724t) terminal dendrites; $p = 0.0414$), supporting a defect in branching. Mutant neurons also had reduced dendrite length (**Fig. 5F,** $p < 0.0001$). GluN2B^{WT} and GluN2B^{724t} -expressing cells appeared to be similar with regard to the number of primary branches (**Fig. 6A**). However, clear differences were observed in intermediate (e.g. tertiary) and terminal dendrite branches (**Fig. 6A**). Deficits in dendrite length were observed throughout the dendritic arbor, regardless of branch order (**Fig. 6B,** primary: 38.09 +/- 3.70µm/dendrite segment (wt) and 26.29 +/- 1.20µm (724t), $p = 0.0014$; secondary: 41.14 +/- 3.70µm (wt) and 24.35 +/- 2.20µm (724t), $p = 8.5 \times 10^{-5}$; tertiary: 50.31 +/- 1.20µm (wt) and 38.67 +/- 1.57µm (724t) terminal: 57.70 +/- 3.49µm (wt) and 42.64 +/- 4.05µm (724t), $p = 4.16 \times 10^{-6}$; n = 12 (wt) and 15 (724t) neurons). The pervasiveness of defects in the dendritic arbors of mutant neurons indicates a severe impairment in dendrite development.

The effect of this ASD-associated mutation in *GRIN2B* appeared to be due to the mutant GluN2B interfering with dendrite growth. The alternative possibility is that over-expression of GluN2B^{WT} enhances dendrite growth, while the mutant is unable to promote growth. In support of the former hypothesis, the prevalence of highly abnormal and dysmorphic dendritic structures upon expression of GluN2B^{724t} suggests that the mutant protein produces a detrimental effect. In addition, when neurons were transfected with GFP-GluN2B^{WT} and then labeled with antibodies against GluN2B, fluorescence intensities of GluN2B from transfected cells and neighboring untransfected neurons indicated that GluN2B^{WT} was not substantially over-expressed in dendrites, consistent with previous reports (Barria and Malinow, 2002; Philpot et al., 2001). Moreover, in contrast to GFP-GluN2B^{724t}, neurons transfected with GFP-GluN2B^{WT} appeared similar to neurons transfected with only GFP (**Fig. S2**). These observations argue against the latter hypothesis. Together, these data suggest that this ASD-associated truncated GluN2B mutant interferes with normal dendrite development, even in the presence of wild-type GluN2B.

To determine whether loss of the extracellular loop was sufficient to produce the underdeveloped and dysmorphic dendrite phenotypes, we also evaluated the effects of the GluN2B$^{\Delta 724\text{-}786}$ mutant on dendrite architecture. The effects of the deletion mutant were qualitatively and quantitatively indistinguishable from those of GluN2B^{724t} (**Fig. 5A-F;** for all comparisons of GluN2B$^{\Delta 724\text{-}786}$ and GluN2B^{724t} mutants, $p > 0.3$). Both underdeveloped and dysmorphic dendritic arbors were prevalent in GluN2B$^{\Delta 724\text{-}786}$-expressing neurons (**Fig. 5A and B**). When compared to GFP-GluN2B^{WT} neurons, GluN2B$^{\Delta 724\text{-}786}$ neurons also had fewer branch points (**Fig. 5D,** 20.80 +/- 1.52µm, $p = 0.0035$), fewer terminal dendrites (**Fig. 5E,** 28.0 +/- 1.96µm, $p = 0.0078$) and reduced dendrite length (**Fig. 5F**, $p < 0.0001$; n = 15 GluN2B$^{\Delta 724\text{-}786}$ neurons and 12 GluN2B^{WT} neurons).

GluN2B mutations do not reduce mTOR activation

The mTOR pathway promotes dendrite growth (Feliciano et al., 2011; Fraser et al., 2008; Gallent and Steward, 2018; Jaworski et al., 2005; Kwon et al., 2006; Meikle et al., 2007; Zhou et al., 2009), and mutations in components of the mTOR pathway can lead to ASD (Gao and Penzes, 2015; Lin et al., 2016; Magdalon et al., 2017). In addition, NMDAR activation, and in particular activation of GluN2B-containing receptors, has been linked to mTOR activation

(Burket et al., 2015; Iafrati et al., 2014; Miller et al., 2014; Wang et al., 2011). Therefore, an important question is whether mutations in GluN2B disrupt dendrite development by interfering with mTOR signaling. Phosphorylation of p70 ribosomal S6 kinase (pS6K) is a standard assay for activation of mTOR signaling, so we tested whether mTOR activity was altered upon expression of GluN2B^{724t}. To account for potential variability across networks, pS6K was quantified by calculating the ratio of pS6K immunofluorescence in GluN2B-transfected neurons versus neighboring untransfected neurons. We analyzed mTOR signaling within the cell body since most of the pS6K signal was localized to the soma. There was no statistically significant difference in the pS6K intensity ratio in GluN2B^{724t} neurons when compared to GluN2B^{WT} neurons (**Fig. 7A-B;** ratio of fluorescence in transfected and untransfected cells: 0.94 +/- 0.12 (wt) and 0.92 +/- 0.17 (724t); p = 0.955; WT: n = 8 transfected and 21 untransfected neurons, 724t: n = 14 transfected and 40 untransfected neurons).

Inhibition of mTOR results in an overall reduction in cell size (Backman et al., 2001; Feliciano et al., 2011; Gallent and Steward, 2018; Kwon et al., 2001; Meikle et al., 2007; Tavazoie et al., 2005). If GluN2B^{724t} alters dendrite growth by disrupting mTOR signaling pathways, we would also expect to observe a reduction in soma size. The soma size was not significantly different between pyramidal-shaped neurons that expressed GluN2B^{WT} or GluN2B^{724t} (**Fig. 7C;** GluN2B^{WT}: 299.112 ± 109.73µm^2, n = 13 and GluN2B^{724t}: 245.8066 ± 59.94 µm^2, n = 15; *p* = 0.1162). Together, these data suggest that GluN2B^{724t} does not persistently decrease mTOR signaling. It remains possible that transient changes in mTOR signaling occurred earlier in development and contribute to the GluN2B^{724t}-dependent reduction in dendrite growth; however, dendrite length was reduced in the newest (terminal) branches, suggesting that the abnormal signaling mechanisms that are directly responsible for the dendrite growth phenotype persists through the age at which mTOR activation was evaluated here.

ASD mutant GluN2B does not alter dendritic spine density or morphology

Since the ASD-associated mutation reduced dendrite arbor length and complexity, we next asked whether development of dendritic spines was also abnormal. To do so, we imaged tdTomato-filled neurons transfected with either GluN2B^{WT} or GluN2B^{724t} then measured dendritic spine densities (**Fig. 8**). Although the overall dendritic spine density for GluN2B^{724t} neurons generally appeared to be lower than GluN2B^{WT} neurons (**Fig. 8A-C**), the apparent

difference was not significant (p = 0.27, one-way ANOVA). Average spine densities per 40µm of dendrite length for GluN2B^{WT}-expressing neurons was 5.7 +/- 0.8 (n = 7 dendrites) and for GluN2B^{724t} -expressing neurons was 4.5 +/- 0.6 (n = 15 dendrites; **Fig. 8C**). Since the GluN2B^{724t} mutation reduced dendrite lengths without an increase in spine density, we infer that GluN2B^{724t} neurons have fewer synapses overall, which may contribute to ASD pathology.

As neurons develop, dendritic spine morphology changes, and it is thought that these changes in morphology reflect spine maturation (Berry and Nedivi, 2017). For example, it is thought that filopodia and stubby spines are immature structures, while mushroom spines are mature. Therefore, we examined spine morphology upon expression of either GluN2B^{WT} or GluN2B^{724t}. Spines were classified as filopodial, thin, stubby, or mushroom. When wild-type and mutant neurons were compared, we did not observe significant differences in the distribution of spines among mature and immature morphological classes (**Fig. 8D;** GluN2B^{WT}: n= 39 spines, GluN2B^{724t}: n= 64 spines). For example, there was no change in either immature forms, such as filopodia and stubby spines (p = 0.6076 and 0.1546, respectively), or in mushroom spines, a mature morphology (p = 0.4272). In contrast, the percentage of spines classified as thin was elevated in neurons expressing GluN2B^{724t} (**Fig. 8D;** GluN2B^{WT}: 12.5 +/- 6.3% of spines, n= 39 spines, GluN2B^{724t}: 40.7 +/- 8.0% of spines, n= 64 spines; p = 0.0354 by ANOVA).

Discussion:

Human and mouse studies suggest that NMDA receptor dysfunction may be a common pathogenic mechanism in ASD (Gao and Penzes, 2015; Uzunova et al., 2014). As a result, the "NMDAR dysfunction hypothesis" of ASD has been proposed (Lee et al., 2015). In most studies of ASD model animals, abnormal NMDAR signaling or expression has been observed as a consequence of mutations in other genes (Gao and Penzes, 2015; Uzunova et al., 2014). Therefore, it is unclear whether altered NMDAR signaling causes ASD or, instead, is an epiphenomenon that does not itself lead to ASD. Here, we directly tested whether NMDARs play a pathogenic role in ASD by investigating the effects of ASD-associated mutations within the GluN2B subunit of NMDARs. We find that an ASD-associated *de novo* mutation eliminates receptor trafficking to the cell surface but not assembly with wild-type receptor subunits, and homozygous mutant receptors completely lack calcium currents. Expression of ASD mutant GluN2B in cortical neurons results in aberrant dendrite arborization. Mutant GluN2B was

sparsely expressed in neurons; therefore, the observed effects on dendrite growth were cell-autonomous. Overall, our results suggest that ASD-associated GluN2B mutations contribute to ASD pathogenesis by interfering with NMDAR signaling and trafficking, which in turn disrupts development of dendrites. Therefore, this study provides strong evidence that NMDA receptor dysfunction plays a direct pathogenic role in ASD by disrupting neuronal development.

Our results indicate that ASD-associated mutations in GluN2B impair dendrite growth and patterning in cortical excitatory neurons. Consistent with our findings, several reports have shown GluN2B-containing receptors are required for normal NMDAR-dependent dendrite growth and refinement, since direct manipulation of GluN2B expression or genetic swapping of GluN2A with GluN2B is sufficient to induce abnormal dendrite architecture in a variety of neuron types (Bustos et al., 2014; Espinosa et al., 2009; Ewald et al., 2008; Keith et al., 2019; Sepulveda et al., 2010). Interestingly, when GluN2B knockout neurons were compared to GluN2B heterozygous neurons *in vivo*, patterning of dendrites was abnormal but dendrite length and branching were unaltered in granule cells and cortical layer 4 spiny stellate cells in barrel cortex (Espinosa et al., 2009). In the case of the ASD-associated mutation studied here, both the length of dendrites and the number of dendrite branches were affected when the mutant receptor was co-expressed with wild-type receptors.

Where does this difference in phenotype come from? Based on the effects of NMDARs and signaling pathways that act down-stream of NMDARs, it has been proposed that regulation of dendritogenesis by NMDARs is cell-type specific (Lohmann and Wong, 2005). The present study targeted cortical pyramidal neurons for analysis, while the knockout study characterized Layer 4 spiny stellate neurons from barrel cortex and dentate gyrus granule cells (Espinosa et al., 2009). Therefore, the cortical neurons studied here could have a stronger dependence on GluN2B-containing receptors, while GluN2B could play less of a role in spiny stellate and granule cells. Importantly, it is widely accepted that cortical pyramidal neurons contribute to ASD pathophysiology (Gao and Penzes, 2015; Varghese et al., 2017), making them an ideal model to investigate the effects of GluN2B mutations.

Abnormal dendrite morphogenesis appears to represent a common cellular phenotype in ASD. Analysis of the brains of individuals with ASD has frequently revealed decreased dendritic arborization (Lin et al., 2016; Varghese et al., 2017). In addition, defective dendrite development has been reported in several mouse models of syndromic ASD and valproate exposure, which dramatically increases risk for ASD (Lin et al., 2016; Martinez-Cerdeno, 2017;

Varghese et al., 2017). Interestingly, ASD-associated mutations in CaMKII interfere with dendrite arborization and prevent binding of CaMKII to GluN2B (Stephenson et al., 2017). Here, we found that dendrite development was impaired by mutations in GluN2B that lead to non-syndromic ASD. Since confounding comorbidities are minimized in non-syndromic ASD, observing this neurodevelopmental phenotype in a model of non-syndromic ASD provides strong support for a role for dendrite maldevelopment in ASD pathophysiology.

Here, the ASD-mutation deletes the cytoplasmic tail of GluN2B, along with the fourth transmembrane domain and a substantial portion of the S2 extracellular loop. It has been shown that the C-terminus of GluN2 is important for regulation of dendrite growth and branching by GluN2B-containing receptors (Bustos et al., 2014; Keith et al., 2019). Residues in the C-terminus of GluN2B and GluN2A are also essential for NMDAR trafficking to dendrites and synapses (Chung et al., 2004; Hawkins et al., 2004; Horak et al., 2008; Mori et al., 1998; Prybylowski et al., 2005; Sans et al., 2003; Steigerwald et al., 2000). In GluN2A, the analogous fourth transmembrane domain (M4) contains residues important for channel gating, and these residues are conserved in GluN2B (Ren et al., 2003). Moreover, receptors with deletion of the M4 domain from GluN2A do not form functional channels (Schorge and Colquhoun, 2003). Therefore, we asked whether the cytoplasmic tail and/or M4 mediate the effects of this ASD mutation on NMDAR trafficking, function and dendrite development. Unexpectedly, we found that deletion of these regions was not necessary for the observed deficits. Instead, deletion of a portion of the S2 extracellular loop was sufficient to reproduce all of the phenotypes observed with the truncation mutant. Consistent with our observations, this portion of the extracellular loop includes residues that are involved in ligand binding, and glutamate binding is necessary for trafficking through the secretory pathway (She et al., 2012).

Recent genetic analysis of *de novo* mutations has identified additional ASD-associated mutations in GluN2B. Consistent with the observations reported here, several of these mutations produce NMDA receptors with reduced or abolished channel properties or trafficking to the cell surface in heterologous expression systems (Adams et al., 2014; Fedele et al., 2018; Liu et al., 2017; Swanger et al., 2016; Vyklicky et al., 2018). It will be important in future studies to compare the effects of distinct ASD mutations on NMDAR trafficking and function within neurons and to determine whether abnormal dendrite development is a common phenotypic outcome of ASD-associated GluN2B mutations.

To date, studies have identified more than 25 disease-associated variations within the S2 extracellular ligand-binding loop and the linker sequences that connect S2 to transmembrane domains 3 and 4 (SFARi gene, July 2019). These mutations may produce cellular phenotypes that are similar to those presented here for GluN2B^{724t} and GluN2B$^{\Delta 724\text{-}786}$. In particular, analogous phenotypes seem likely for variants with predicted truncations within this region: c.2131C>T, which produces a premature stop at amino acid 711 (Kenny et al., 2014) and c.2384_2391del, which produces a premature stop at amino acid 795 (Stessman et al., 2017). A variant c.2539C>T, predicted to truncate GluN2B at amino acid 847 within the 4th transmembrane domain (Platzer et al., 2017) and the splice site variant c.2360-2A>G (Endele et al., 2010) may result in similar effects, as well. Moreover, in future studies, it will be interesting to determine whether any mutation that interferes with glutamate binding produces deficits in subcellular trafficking and dendrite morphogenesis, as observed for GluN2B^{724t}.

The detrimental effect of mutant GluN2B on dendrite growth in the presence of two copies of normal wild-type *GRIN2B* raises the question of whether ASD-associated GRIN2B mutations act via a dominant-negative mechanism, a gain of toxic function, or haploinsufficiency. As individuals with ASD-associated *de novo* mutations are heterozygous for the disrupting mutation, it is widely assumed that these mutations will result in haploinsufficiency for the mutated gene. However, our data demonstrate that mutant GluN2B impairs dendrite growth in the presence of two copies of normal wild-type *GRIN2B.* Furthermore, loss of one *GRIN2B* allele in heterozygous knockout mice does not significantly reduce GluN2B-dependent post-synaptic responses (Espinosa et al., 2009). Together, these observations argue against a simple haploinsufficiency mechanism. To distinguish between dominant-negative mechanisms and toxic gain-of-function, it will be necessary to determine whether wild-type NMDAR function or localization are impaired upon expression of mutant GluN2B. In addition, it will be important to consider both ionotropic and unconventional, ion flux-independent functions of NMDARs (Burket and Deutsch, 2019; Dore et al., 2017; Keith et al., 2019; Montes de Oca Balderas, 2018) (Keith et al., 2019; Montes de Oca Balderas, 2018; Burket, 2019; Dore et al., 2017). Regardless of the specific mechanism involved, the differences between expression of GluN2B bearing a specific ASD mutation and heterozygous deletion of *GRIN2B* underscores the importance of evaluating specific ASD-associated mutations when investigating etiological mechanisms of ASD.

We observed reduced dendrite arbor length and complexity, which is expected to alter neural circuit function by changing dendrite cable properties (Lefebvre et al., 2015). Future studies should be aimed at directly measuring the effects of GluN2B mutations and the resulting dendrite maldevelopment on dendrite cable properties. In addition, this study focuses on cortical excitatory neurons since they are the principal neurons responsible for carrying feed-forward information within the cerebral cortex. In order to understand the ultimate impact on circuit function, it will also be important in the future to determine whether similar changes are observed in cortical inhibitory neurons and whether excitatory/inhibitory balance is shifted.

Understanding the precise mechanisms of action of individual mutations in strong candidate ASD genes is essential to unraveling the complex etiology that leads to ASD. Studying individual mutations will help the field move toward identifying core neurodevelopmental phenotypes that characterize ASD or subtypes of ASD. In addition, understanding common phenotypes will be informative with regards to which potential therapeutic approaches might be beneficial for individual patients. For example, augmenting the activity of GluN2B-containing receptors might be beneficial in the case of mutations that severely disrupt NMDAR function, signaling pathways activated by NMDARs or dendrite development.

Materials and Methods

All studies were conducted with an approved protocol from the Case Western Reserve University Institutional Animal Care and Use Committee or the Central Michigan University Institutional Animal Care and Use Committee, in compliance with the National Institutes of Health guidelines for care and use of experimental animals.

cDNA constructs

pEGFP-GluN2B was a gift from Stefano Vicini (Addgene plasmid # 17925; (Luo et al., 2002)). GFP is inserted in the amino-terminal extracellular domain after the signal peptide. GluN1-HcRed and GluN1-CFP were from Phillip Washbourne. Untagged GluN2B, GluN2A and GluN1 were gifts of John Woodward. tdTomato-N1 was from Michael Davidson & Roger Tsien (Addgene plasmid # 54642).

Generation of mutant GluN2B

Mutant GluN2B cDNA constructs were made from pEGP-GluN2B using the Q5 Site-directed Mutagenesis Kit (New England Biolabs). For GluN2B^{724t}, a stop site was introduced using the following primers, designed using NEBaseChanger (New England Biolabs): 5'-GAAAACAGGGTACGCTTGATGCATTC-3' and 5'-AGGGAGAGCAATGCATCATC-3'. Mutations were confirmed by sequencing.

HEK Cell culture and Transfection

HEK-293 cells (ATCC, low passage) were cultured in Dulbecco's Modified Eagle's Medium (Invitrogen or HyClone) supplemented with 10% fetal bovine serum (Invitrogen or HyClone), penicillin and streptomycin (Invitrogen) and maintained at 5% CO_2. HEK cells were used at a low passage number and displayed appropriate morphology. For imaging, HEK cells were plated on poly-lysine-coated glass coverslips (Carolina Scientific). HEK-293 cells were transfected using Lipofectamine 2000 (Invitrogen) in the absence of antibiotics, essentially as previously described (Bury and Sabo; Bury and Sabo, 2014; Gill et al., 2015). To prevent excitotoxicity, kynurenate (1 mM) or ketamine (1 µg/mL) was added at the time of transfection. Cells were used in assays at 24-72h after transfection.

Neuronal Cell Culture and Transfection:

Neurons and astrocytes were derived from the cortices of wild-type Sprague Dawley rats of both sexes at 0-1 days postnatal. Neurons were dissociated and grown on a confluent monolayer of astrocytes, as previously described (Bury and Sabo, 2011; Bury and Sabo, 2014; Sceniak et al., 2012). Neurons were maintained at 5% CO_2 in Neurobasal medium (Invitrogen) with B27 supplement (Invitrogen). Neurons were transfected at two days *in vitro* (DIV) using the calcium phosphate method (Berry et al., 2012) with 2.6 µg GluN2B DNA/18mm coverslip. Neurons were co-transfected with tdTomato (0.4 µg DNA/coverslip) to fill transfected cells. For some surface localization experiments, neurons were transfected at 3DIV with GFP-GluN2B. Transfection efficiency was sufficiently low that a large majority of transfected neurons were excitatory neurons, based on pyramidal-shaped somas and spiny dendrites.

Calcium Imaging

HEK-293 cells were loaded with 5 uM Fluo4-AM (Invitrogen) for 30 minutes at room temperature. Imaging was performed in magnesium-free artificial cerebrospinal fluid (ACSF; 120 mM NaCl, 3 mM KCl, 2 mM $CaCl_2$, 30 mM D-glucose, 20 mM HEPES, and 0.2% sorbitol, pH 7.3). For each condition, 60 images were collected at a rate of 1 frame per second. Stimulation was via perfusion with ACSF containing NMDA (100 uM) in the presence of glycine (10 uM). After washout, stimulation was repeated in the presence of ketamine (1µg/mL). Only healthy cells, based on morphology in differential interference contrast images, were selected for analysis, and health assessments were made while blind to fluorescence.

Immunocytochemistry

Immunocytochemistry was generally performed on neurons at 10-14 DIV. In most cases, neurons were fixed with 4% paraformaldehyde and 0.32M sucrose in phosphate-buffered saline and then permeabilized using 0.1% Triton-X-100 in PBS. For GluN1 immunolabeling, neurons were fixed in -20C methanol then permeabilized in triton X-100 (0.025%). After blocking with 10% horse serum or bovine serum albumin, neurons were labeled with primary antibodies, applied overnight at 4°C in the presence of 3% horse serum or bovine serum albumin. Primary antibodies were chicken anti-GFP (1:2500; Millipore), rabbit anti-GFP (1:2000; Invitrogen); mouse anti-GluN1 (Millipore); rabbit anti-GluN2B (1:300, Alomone); rabbit anti-phosphorylated S6 (1:800; Cell Signaling Technologies); chicken anti-MAP2 (1:2000; Millipore), and mouse anti-Beta-III Tubulin (1:200; Millipore). Secondary antibodies were Alexa conjugates (Invitrogen). Coverslips were mounted in Fluoromount (Fisher Scientific, Pittsburgh, PA, USA) containing DABCO (1,4-diazabicyclo[2.2.2] octane) (Sigma, St Louis, MO, USA).

For surface labeling of HEK cells, cells were incubated with rabbit anti-GFP (Invitrogen) and then Alexa 633-conjugated anti-rabbit (Invitrogen) antibodies for 30 min at 4C or chicken anti-GFP followed by Alexa 550-conjugated anti-chicken antibodies. The cells were then fixed for 15 minutes in 4% paraformaldehyde in phosphate-buffered saline (PBS) containing 4% sucrose. For surface labeling of neurons, primary antibodies were applied to living neurons prior to fixation, and secondary antibodies were applied after fixation. Neuronal surface immunofluorescence images were collected at 6-13 DIV.

Fluorescence was not observed in the absence of primary antibody. Labeling was absent with anti-GFP antibodies when cells were not transfected. Untransfected HEK-293 cells did not display fluorescence with GluN1 and GluN2B antibodies.

Fluorescence Microscopy and Image analysis

Cells were imaged with a Nikon C1 Plus confocal system with an Eclipse Ti-E microscope. Lasers were 488 nm argon, 543 nm helium-neon, and 633 nm helium-neon. Detection filters were 515/30 nm bandpass, 590/50 nm bandpass, and 650 LP. Some images were collected using a Nikon C2 plus confocal system with an Ni-E microscope, 405/488/561/640 nm diode lasers and 525/50 nm bandpass, 600/50 nm bandpass, and 660 LP detection filters. For live time-lapse imaging, a perfect focus system was used to maintain focus. For both systems, objectives used were 60x (1.4 NA), 20X (NA 0.75) or 40× (0.95 NA) Plan Apo objectives

Large neurons with pyramidal somas were chosen for analysis. These were likely excitatory neurons since they were pyramidal and spiny. Only healthy cells were imaged, as determined by the appearance of the soma under differential interference contrast and a smooth axon without fragmentation or blebbing. Within a given experiment, neurons were also chosen with similar transfection levels, as judged by tdTomato and GFP fluorescence. Stacks of images (Z-stacks) were taken in order to span the entire cell volume. Gains were set to avoid saturation and kept constant during imaging of each experiment when intensities, morphologies or areas were quantified. All channels were imaged separately and sequentially to avoid bleed through. Images were taken with pixel sizes ranging from 90 (for synaptic structures) to 207nm (for imaging complete dendritic arbors).

Sholl Analysis

Sholl analysis was conducted essentially as previously described (Kutzing et al., 2010; Langhammer et al., 2010; O'Neill et al., 2015). Dendrites were manually traced in NeuronJ based on cytosolic tdTomato fills, while the user was blind to condition. Traces were transferred to BonFire for further analysis. Dendrites were considered to be extensions that were at least 10 µm long. Primary dendrites emanate directly from the soma, while remaining orders are defined by the successive branch points between the soma and the relevant dendrite.

Dendritic Spine Analysis

Dendritic spines were measured in Z-projections from secondary and occasionally tertiary dendrite branches of pyramidal neurons. Dendrite segments were generally clear from intersecting branches and at least 40 μ m in length. Spines were analyzed by blind observers using ImageJ/Fiji. Dendritic spines were counted in a semi-automatic manner, as previously described (Orlowski and Bjarkam, 2012). Briefly,images of tdTomato fills were automatically thresholded using the ImageJ *Threshold* function. Then, dendrites and spines were automatically detected by using two sequential applications of the *Skeletonize* function in ImageJ. Dendritic spine lengths and widths were measured manually using ImageJ. Any dendritic protrusions over 10 μ m in length or not clearly focused within the imaged volume were discarded from the analysis. Spine morphologies were classified as filopodial, long thin, thin, stubby, mushroom and branched based on length, width, and length:width ratios, as previously described (Risher et al., 2014). Briefly, filopodia were defined as having lengths greater than 2 μ m; stubby spines had length:width ratios less than 1; mushroom spines had widths greater than 0.6 μ m; and thin spines had lengths less than 2 μ m and length:width ratios greater than 1.

Co-Immunoprecipitation and Immunoblotting

Transfected cells were lysed on ice for 30 min in lysis buffer (50 mM Tris [pH 7.4], 150 mM NaCl, 2 mM EGTA, 1% Triton X-100, and protease and phosphatase inhibitors). The 20,000 X g supernatant was then incubated with rabbit anti-GFP antibodies followed by protein A/G agarose beads that had been pre-washed with lysate. Bound proteins were subjected to SDS-PAGE, using 4-20% Tris-glycine gels (Life Technologies), then transferred to nitrocellulose membranes. After blocking with 10% nonfat dry milk in Tris-buffered saline with Tween-20, membranes were probed with rabbit-anti-GFP, mouse anti-GluN1 and IRDye-conjugated secondary antibodies (LiCor, Lincoln, NE) or HRP-conjugated (BioRad) secondary antibodies. Blots were imaged using a LiCor Odyssey imaging system or chemiluminescence.

Data Analysis

Images were analyzed using custom-written macros and functions in ImageJ and Matlab (Mathworks). These macros are available via email request. Maximum intensity projections were created, and individual transfected cells or regions of interest were outlined based on fluorescent fills and image statistics. Mean fluorescence intensity was measured for each

channel quantified. Fluorescence intensity data were analyzed for statistical significance using ANOVA, with Fisher's PLSD post-hoc tests. Multiple comparisons corrections were applied where appropriate (Figures 5 and 6) using Matlab's "multcompare" function with Bonferroni corrections. Spine densities were compared by one-way ANOVA, and spine morphology types were compared through ANOVA with Bonferroni's multiple comparisons correction.

Acknowledgements: We thank Jacob Bahry for helpful reading of the manuscript. We thank Sahil Patel, Natuwa Basalirwa and Jessica Lahr for technical assistance. This work was supported by a Research Starter grant from the Simons Foundation Autism Research Initiative.

The authors declare that they have no competing interests.

Author contributions: KNF, QW, SD, SP, KB and SLS performed experiments and collected data. MPS, KNF, QW, KB, LP, JWZ and SLS analyzed data and wrote the paper.

References:

Adams, D. R., Yuan, H., Holyoak, T., Arajs, K. H., Hakimi, P., Markello, T. C., Wolfe, L. A., Vilboux, T., Burton, B. K., Fajardo, K. F., et al. (2014). Three rare diseases in one Sib pair: RAI1, PCK1, GRIN2B mutations associated with Smith–Magenis Syndrome, cytosolic PEPCK deficiency and NMDA receptor glutamate insensitivity. *Mol. Genet. Metab.* **113**, 161–170.

Asaka, Y., Jugloff, D. G. M., Zhang, L., Eubanks, J. H. and Fitzsimonds, R. M. (2006). Hippocampal synaptic plasticity is impaired in the Mecp2-null mouse model of Rett syndrome. *Neurobiol. Dis.* **21**, 217–227.

Backman, S. A., Stambolic, V., Suzuki, A., Haight, J., Elia, A., Pretorius, J., Tsao, M. S., Shannon, P., Bolon, B., Ivy, G. O., et al. (2001). Deletion of Pten in mouse brain causes seizures, ataxia and defects in soma size resembling Lhermitte-Duclos disease. *Nat. Genet.* **29**, 396–403.

Barria, A. and Malinow, R. (2002). Subunit-specific NMDA receptor trafficking to synapses. *Neuron* **35**, 345–353.

Berg, L. K., Larsson, M., Morland, C. and Gundersen, V. (2013). Pre- and postsynaptic localization of NMDA receptor subunits at hippocampal mossy fibre synapses. *Neuroscience* **230**, 139–150.

Berry, K. P. and Nedivi, E. (2017). Spine Dynamics: Are They All the Same? *Neuron* **96**, 43–55.

Berry, C. T., Sceniak, M. P., Zhou, L. and Sabo, S. L. (2012). Developmental up-regulation of vesicular glutamate transporter-1 promotes neocortical presynaptic terminal development. *PLoS One* **7**, e50911.

Bostrom, C. A., Majaess, N.-M., Morch, K., White, E., Eadie, B. D. and Christie, B. R. (2015). Rescue of NMDAR-dependent synaptic plasticity in Fmr1 knock-out mice. *Cereb. Cortex* **25**, 271–279.

Bourgeron, T. (2009). A synaptic trek to autism. *Curr Opin Neurobiol* **19**, 231–234.

Burket, J. A. and Deutsch, S. I. (2019). Metabotropic functions of the NMDA receptor and an evolving rationale for exploring NR2A-selective positive allosteric modulators for the treatment of autism spectrum disorder. *Prog. Neuropsychopharmacol. Biol. Psychiatry* **90**, 142–160.

Burket, J. A., Benson, A. D., Tang, A. H. and Deutsch, S. I. (2015). NMDA receptor activation regulates sociability by its effect on mTOR signaling activity. *Prog. Neuropsychopharmacol. Biol. Psychiatry* **60**, 60–65.

Bury, L. A. and Sabo, S. L. (2011). Coordinated trafficking of synaptic vesicle and active zone proteins prior to synapse formation. *Neural Dev* **6**, 24.

Bury, L. A. and Sabo, S. L. (2014). Dynamic mechanisms of neuroligin-dependent presynaptic terminal assembly in living cortical neurons. *Neural Dev.* **9**, 13.

Bustos, F. J., Varela-Nallar, L., Campos, M., Henriquez, B., Phillips, M., Opazo, C., Aguayo, L. G., Montecino, M., Constantine-Paton, M., Inestrosa, N. C., et al. (2014). PSD95 suppresses dendritic arbor development in mature hippocampal neurons by occluding the clustering of NR2B-NMDA receptors. *PLoS One* **9**, e94037.

Charton, J. P., Herkert, M., Becker, C. M. and Schroder, H. (1999). Cellular and subcellular localization of the 2B-subunit of the NMDA receptor in the adult rat telencephalon. *Brain Res.* **816**, 609–617.

Chung, H. J., Huang, Y. H., Lau, L.-F. and Huganir, R. L. (2004). Regulation of the NMDA receptor complex and trafficking by activity-dependent phosphorylation of the NR2B subunit PDZ ligand. *J. Neurosci.* **24**, 10248–59.

De Filippis, B., Valenti, D., Chiodi, V., Ferrante, A., de Bari, L., Fiorentini, C., Domenici, M. R., Ricceri, L., Vacca, R. A., Fabbri, A., et al. (2015). Modulation of Rho GTPases rescues brain mitochondrial dysfunction, cognitive deficits and aberrant synaptic plasticity in female mice modeling Rett syndrome. *Eur. Neuropsychopharmacol.* **25**, 889–901.

De Rubeis, S., He, X., Goldberg, A. P., Poultney, C. S., Samocha, K., Ercument Cicek, A., Kou, Y., Liu, L., Fromer, M., Walker, S., et al. (2014). Synaptic, transcriptional and chromatin genes disrupted in autism. *Nature* **515**, 209–15.

DeBiasi, S., Minelli, A., Melone, M. and Conti, F. (1996). Presynaptic NMDA receptors in the neocortex are both auto- and heteroreceptors. *Neuroreport* **7**, 2773–2776.

Dore, K., Stein, I. S., Brock, J. A., Castillo, P. E., Zito, K. and Sjostrom, P. J. (2017). Unconventional NMDA Receptor Signaling. *J. Neurosci.* **37**, 10800–10807.

Endele, S., Rosenberger, G., Geider, K., Popp, B., Tamer, C., Stefanova, I., Milh, M., Kortum, F., Fritsch, A., Pientka, F. K., et al. (2010). Mutations in GRIN2A and GRIN2B encoding regulatory subunits of NMDA receptors cause variable neurodevelopmental phenotypes. *Nat Genet* **42**, 1021–1026.

Espinosa, J. S., Wheeler, D. G., Tsien, R. W. and Luo, L. (2009). Uncoupling dendrite growth and patterning: single-cell knockout analysis of NMDA receptor 2B. *Neuron* **62**, 205–217.

Etherton, M., Foldy, C., Sharma, M., Tabuchi, K., Liu, X., Shamloo, M., Malenka, R. C., Sudhof, T. C., Földy, C. and Südhof, T. C. (2011). Autism-linked neuroligin-3 R451C mutation differentially alters hippocampal and cortical synaptic function. *Proc Natl Acad Sci U S A* **108**, 13764–13769.

Ewald, R. C., Van Keuren-Jensen, K. R., Aizenman, C. D. and Cline, H. T. (2008). Roles of NR2A and NR2B in the development of dendritic arbor morphology in vivo. *J. Neurosci.* **28**, 850–61.

Fedele, L., Newcombe, J., Topf, M., Gibb, A., Harvey, R. J. and Smart, T. G. (2018). Disease-associated missense mutations in GluN2B subunit alter NMDA receptor ligand binding and ion channel properties. *Nat. Commun.* **9**, 957.

Feliciano, D. M., Su, T., Lopez, J., Platel, J.-C. and Bordey, A. (2011). Single-cell Tsc1 knockout during corticogenesis generates tuber-like lesions and reduces seizure threshold in mice. *J. Clin. Invest.* **121**, 1596–1607.

Fraser, M. M., Bayazitov, I. T., Zakharenko, S. S. and Baker, S. J. (2008). Phosphatase and tensin homolog, deleted on chromosome 10 deficiency in brain causes defects in synaptic structure, transmission and plasticity, and myelination abnormalities. *Neuroscience* **151**, 476–488.

Gallent, E. A. and Steward, O. (2018). Neuronal PTEN deletion in adult cortical neurons triggers progressive growth of cell bodies, dendrites, and axons. *Exp. Neurol.* **303**, 12–28.

Gao, R. and Penzes, P. (2015). Common mechanisms of excitatory and inhibitory imbalance in schizophrenia and autism spectrum disorders. *Curr. Mol. Med.* **15**, 146–167.

Gill, I., Droubi, S., Giovedi, S., Fedder, K. N., Bury, L. A. D., Bosco, F., Sceniak, M. P., Benfenati, F. and Sabo, S. L. (2015). Presynaptic NMDA receptors - dynamics and distribution in developing axons in vitro and in vivo. *J. Cell Sci.* **128**, 768–780.

Hamada, S., Ogawa, I., Yamasaki, M., Kiyama, Y., Kassai, H., Watabe, A. M., Nakao, K., Aiba, A., Watanabe, M. and Manabe, T. (2014). The glutamate receptor GluN2 subunit regulates synaptic trafficking of AMPA receptors in the neonatal mouse brain. *Eur. J. Neurosci.* **40**, 3136–3146.

Hawkins, L. M., Prybylowski, K., Chang, K., Moussan, C., Stephenson, F. A. and Wenthold, R. J. (2004). Export from the endoplasmic reticulum of assembled N-methyl-d-aspartic acid receptors is controlled by a motif in the c terminus of the NR2 subunit. *J. Biol. Chem.* **279**, 28903–10.

Horak, M., Chang, K. and Wenthold, R. J. (2008). Masking of the endoplasmic reticulum retention signals during assembly of the NMDA receptor. *J Neurosci* **28**, 3500–3509.

Horak, M., Petralia, R. S., Kaniakova, M. and Sans, N. (2014). ER to synapse trafficking of NMDA receptors. *Front. Cell. Neurosci.* **8**, 394.

Iafrati, J., Orejarena, M. J., Lassalle, O., Bouamrane, L., Gonzalez-Campo, C. and Chavis, P. (2014). Reelin, an extracellular matrix protein linked to early onset psychiatric diseases, drives postnatal development of the prefrontal cortex via GluN2B-NMDARs and the mTOR pathway. *Mol. Psychiatry* **19**, 417–426.

Iossifov, I., O'Roak, B. J., Sanders, S. J., Ronemus, M., Krumm, N., Levy, D., Stessman, H. A., Witherspoon, K. T., Vives, L., Patterson, K. E., et al. (2014). The contribution of de novo coding mutations to autism spectrum disorder. *Nature* **515**, 216–21.

Jaworski, J., Spangler, S., Seeburg, D. P., Hoogenraad, C. C. and Sheng, M. (2005). Control of dendritic arborization by the phosphoinositide-3'-kinase-Akt-mammalian target of rapamycin pathway. *J. Neurosci.* **25**, 11300–11312.

Jourdain, P., Bergersen, L. H., Bhaukaurally, K., Bezzi, P., Santello, M., Domercq, M., Matute, C., Tonello, F., Gundersen, V. and Volterra, A. (2007). Glutamate exocytosis from astrocytes controls synaptic strength. *Nat. Neurosci.* **10**, 331–339.

Keith, R. E., Azcarate, J. M., Keith, M. J., Hung, C. W., Badakhsh, M. F. and Dumas, T. C. (2019). Direct Intracellular Signaling by the Carboxy terminus of NMDA Receptor GluN2 Subunits Regulates Dendritic Morphology in Hippocampal CA1 Pyramidal Neurons. *Neuroscience* **396**, 138–153.

Kenny, E. M., Cormican, P., Furlong, S., Heron, E., Kenny, G., Fahey, C., Kelleher, E., Ennis, S., Tropea, D., Anney, R., et al. (2014). Excess of rare novel loss-of-function variants in synaptic genes in schizophrenia and autism spectrum disorders. *Mol. Psychiatry* **19**, 872–879.

Komuro, H. and Rakic, P. (1993). Modulation of neuronal migration by NMDA receptors. *Science* **260**, 95–97.

Krueger, D. D., Osterweil, E. K., Chen, S. P., Tye, L. D. and Bear, M. F. Cognitive dysfunction and prefrontal synaptic abnormalities in a mouse model of fragile X syndrome. *Proc Natl Acad Sci U S A* **108**, 2587–2592.

Krumm, N., O'Roak, B. J., Shendure, J. and Eichler, E. E. (2014). A de novo convergence of autism genetics and molecular neuroscience. *Trends Neurosci.* **37**, 95–105.

Kutsuwada, T., Sakimura, K., Manabe, T., Takayama, C., Katakura, N., Kushiya, E., Natsume, R., Watanabe, M., Inoue, Y., Yagi, T., et al. (1996). Impairment of suckling response, trigeminal neuronal pattern formation, and hippocampal LTD in NMDA receptor epsilon 2 subunit mutant mice. *Neuron* **16**, 333–44.

Kutzing, M. K., Langhammer, C. G., Luo, V., Lakdawala, H. and Firestein, B. L. (2010). Automated Sholl analysis of digitized neuronal morphology at multiple scales. *J. Vis. Exp.*

Kwon, C. H., Zhu, X., Zhang, J., Knoop, L. L., Tharp, R., Smeyne, R. J., Eberhart, C. G., Burger, P. C. and Baker, S. J. (2001). Pten regulates neuronal soma size: a mouse model of Lhermitte-Duclos disease. *Nat. Genet.* **29**, 404–411.

Kwon, C. H., Luikart, B. W., Powell, C. M., Zhou, J., Matheny, S. A., Zhang, W., Li, Y., Baker, S. J. and Parada, L. F. (2006). Pten regulates neuronal arborization and social interaction in mice. *Neuron* **50**, 377–388.

Langhammer, C. G., Previtera, M. L., Sweet, E. S., Sran, S. S., Chen, M. and Firestein, B. L. (2010). Automated Sholl analysis of digitized neuronal morphology at multiple scales: Whole cell Sholl analysis versus Sholl analysis of arbor subregions. *Cytometry. A* **77**, 1160–1168.

Larsen, R. S., Corlew, R. J., Henson, M. A., Roberts, A. C., Mishina, M., Watanabe, M., Lipton, S. A., Nakanishi, N., Perez-Otano, I., Weinberg, R. J., et al. NR3A-containing NMDARs promote neurotransmitter release and spike timing-dependent plasticity. *Nat Neurosci* **14**, 338–344.

Larsen, R. S., Smith, I. T., Miriyala, J., Han, J. E., Corlew, R. J., Smith, S. L. and Philpot, B. D. (2014). Synapse-specific control of experience-dependent plasticity by presynaptic NMDA receptors. *Neuron* **83**, 879–893.

Lee, S., Kim, W., Ham, B.-J., Chen, W., Bear, M. F. and Yoon, B.-J. (2008). Activity-dependent NR2B expression is mediated by MeCP2-dependent epigenetic regulation. *Biochem. Biophys. Res. Commun.* **377**, 930–4.

Lee, E.-J., Choi, S. Y. and Kim, E. (2015). NMDA receptor dysfunction in autism spectrum disorders. *Curr. Opin. Pharmacol.* **20**, 8–13.

Lefebvre, J. L., Sanes, J. R. and Kay, J. N. (2015). Development of dendritic form and function. *Annu. Rev. Cell Dev. Biol.* **31**, 741–777.

Lin, Y.-C., Frei, J. A., Kilander, M. B. C., Shen, W. and Blatt, G. J. (2016). A Subset of Autism-Associated Genes Regulate the Structural Stability of Neurons. *Front. Cell. Neurosci.* **10**, 263.

Liu, S., Zhou, L., Yuan, H., Vieira, M., Sanz-Clemente, A., Badger, J. D. 2nd, Lu, W., Traynelis, S. F. and Roche, K. W. (2017). A Rare Variant Identified Within the GluN2B C-Terminus in a Patient with Autism Affects NMDA Receptor Surface Expression and Spine Density. *J. Neurosci.* **37**, 4093–4102.

Lohmann, C. and Wong, R. O. (2005). Regulation of dendritic growth and plasticity by local and global calcium dynamics. *Cell Calcium* **37**, 403–409.

Luo, J.-H. H., Fu, Z.-Y. Y., Losi, G., Kim, B. G., Prybylowski, K., Vissel, B. and Vicini, S. (2002). Functional expression of distinct NMDA channel subunits tagged with green fluorescent protein in hippocampal neurons in culture. *Neuropharmacology* **42**, 306–318.

Magdalon, J., Sanchez-Sanchez, S. M., Griesi-Oliveira, K. and Sertie, A. L. (2017). Dysfunctional mTORC1 Signaling: A Convergent Mechanism between Syndromic and Nonsyndromic Forms of Autism Spectrum Disorder? *Int. J. Mol. Sci.* **18**,.

Martinez-Cerdeno, V. (2017). Dendrite and spine modifications in autism and related neurodevelopmental disorders in patients and animal models. *Dev. Neurobiol.* **77**, 393–404.

McGuinness, L., Taylor, C., Taylor, R. D., Yau, C., Langenhan, T., Hart, M. L., Christian, H., Tynan, P. W., Donnelly, P. and Emptage, N. J. (2010). Presynaptic NMDARs in the hippocampus facilitate transmitter release at theta frequency. *Neuron* **68**, 1109–1127.

Meikle, L., Talos, D. M., Onda, H., Pollizzi, K., Rotenberg, A., Sahin, M., Jensen, F. E. and Kwiatkowski, D. J. (2007). A mouse model of tuberous sclerosis: neuronal loss of Tsc1 causes dysplastic and ectopic neurons, reduced myelination, seizure activity, and limited survival. *J. Neurosci.* **27**, 5546–5558.

Mierau, S. B., Patrizi, A., Hensch, T. K. and Fagiolini, M. (2016). Cell-Specific Regulation of N-Methyl-D-Aspartate Receptor Maturation by Mecp2 in Cortical Circuits. *Biol. Psychiatry* **79**, 746–754.

Miller, O. H., Yang, L., Wang, C.-C., Hargroder, E. A., Zhang, Y., Delpire, E. and Hall, B. J. (2014). GluN2B-containing NMDA receptors regulate depression-like behavior and are critical for the rapid antidepressant actions of ketamine. *Elife* **3**, e03581.

Montes de Oca Balderas, P. (2018). Flux-Independent NMDAR Signaling: Molecular Mediators, Cellular Functions, and Complexities. *Int. J. Mol. Sci.* **19**,.

Monyer, H., Burnashev, N., Laurie, D. J., Sakmann, B. and Seeburg, P. H. (1994). Developmental and regional expression in the rat brain and functional properties of four NMDA receptors. *Neuron* **12**, 529–40.

Mori, H., Manabe, T., Watanabe, M., Satoh, Y., Suzuki, N., Toki, S., Nakamura, K., Yagi, T., Kushiya, E., Takahashi, T., et al. (1998). Role of the carboxy-terminal region of the GluR epsilon2 subunit in synaptic localization of the NMDA receptor channel. *Neuron* **21**, 571–580.

Myers, R. A., Casals, F., Gauthier, J., Hamdan, F. F., Keebler, J., Boyko, A. R., Bustamante, C. D., Piton, A. M., Spiegelman, D., Henrion, E., et al. (2011). A population genetic approach to mapping neurological disorder genes using deep resequencing. *PLoS Genet.* **7**, e1001318.

O'Neill, K. M., Akum, B. F., Dhawan, S. T., Kwon, M., Langhammer, C. G. and Firestein, B. L. (2015). Assessing effects on dendritic arborization using novel Sholl analyses. *Front. Cell. Neurosci.* **9**, 285.

O'Roak, B. J., Deriziotis, P., Lee, C., Vives, L., Schwartz, J. J., Girirajan, S., Karakoc, E., MacKenzie, A. P., Ng, S. B., Baker, C., et al. (2011). Exome sequencing in sporadic autism spectrum disorders identifies severe de novo mutations. *Nat. Genet.* **43**, 585–589.

O'Roak, B. J., Vives, L., Girirajan, S., Karakoc, E., Krumm, N., Coe, B. P., Levy, R., Ko, A., Lee, C., Smith, J. D., et al. (2012a). Sporadic autism exomes reveal a highly interconnected protein network of de novo mutations. *Nature* **485**, 246–250.

O'Roak, B. J., Vives, L., Fu, W., Egertson, J. D., Stanaway, I. B., Phelps, I. G., Carvill, G., Kumar, A., Lee, C., Ankenman, K., et al. (2012b). Multiplex targeted sequencing identifies recurrently mutated genes in autism spectrum disorders. *Science* **338**, 1619–22.

O'Roak, B. J., Stessman, H. A., Boyle, E. A., Witherspoon, K. T., Martin, B., Lee, C., Vives, L., Baker, C., Hiatt, J. B., Nickerson, D. A., et al. (2014). Recurrent de novo mutations implicate novel genes underlying simplex autism risk. *Nat. Commun.* **5**, 5595.

Orlowski, D. and Bjarkam, C. R. (2012). A simple reproducible and time saving method of semi-automatic dendrite spine density estimation compared to manual spine counting. *J. Neurosci. Methods* **208**, 128–133.

Pan, Y., Chen, J., Guo, H., Ou, J., Peng, Y., Liu, Q., Shen, Y., Shi, L., Liu, Y., Xiong, Z., et al. (2015). Association of genetic variants of GRIN2B with autism. *Sci. Rep.* **5**, 8296.

Philpot, B. D., Weisberg, M. P., Ramos, M. S., Sawtell, N. B., Tang, Y. P., Tsien, J. Z. and Bear, M. F. (2001). Effect of transgenic overexpression of NR2B on NMDA receptor function and synaptic plasticity in visual cortex. *Neuropharmacology* **41**, 762–770.

Platzer, K., Yuan, H., Schutz, H., Winschel, A., Chen, W., Hu, C., Kusumoto, H., Heyne, H. O., Helbig, K. L., Tang, S., et al. (2017). GRIN2B encephalopathy: novel findings on phenotype, variant clustering, functional consequences and treatment aspects. *J. Med. Genet.* **54**, 460–470.

Prybylowski, K., Chang, K., Sans, N., Kan, L., Vicini, S. and Wenthold, R. J. (2005). The synaptic localization of NR2B-containing NMDA receptors is controlled by interactions with PDZ proteins and AP-2. *Neuron* **47**, 845–57.

Ren, H., Honse, Y., Karp, B. J., Lipsky, R. H. and Peoples, R. W. (2003). A site in the fourth membrane-associated domain of the N-methyl-D-aspartate receptor regulates desensitization and ion channel gating. *J. Biol. Chem.* **278**, 276–83.

Risher, W. C., Ustunkaya, T., Singh Alvarado, J. and Eroglu, C. (2014). Rapid Golgi analysis method for efficient and unbiased classification of dendritic spines. *PLoS One* **9**, e107591.

Roullet, F. I., Wollaston, L., Decatanzaro, D. and Foster, J. A. (2010). Behavioral and molecular changes in the mouse in response to prenatal exposure to the anti-epileptic drug valproic acid. *Neuroscience* **170**, 514–522.

Sanders, S. J., He, X., Willsey, A. J., Ercan-Sencicek, A. G., Samocha, K. E., Cicek, A. E., Murtha, M. T., Bal, V. H., Bishop, S. L., Dong, S., et al. (2015). Insights into Autism Spectrum Disorder Genomic Architecture and Biology from 71 Risk Loci. *Neuron* **87**, 1215–1233.

Sans, N., Prybylowski, K., Petralia, R. S., Chang, K., Wang, Y. X., Racca, C., Vicini, S. and Wenthold, R. J. (2003). NMDA receptor trafficking through an interaction between PDZ proteins and the exocyst complex. *Nat Cell Biol* **5**, 520–530.

Sanz-Clemente, A., Nicoll, R. A. and Roche, K. W. (2013). Diversity in NMDA receptor composition: many regulators, many consequences. *Neuroscientist* **19**, 62–75.

Sceniak, M. P., Berry, C. T. and Sabo, S. L. (2012). Facilitation of neocortical presynaptic terminal development by NMDA receptor activation. *Neural Dev* **7**, 8.

Sceniak, M. P., Lang, M., Enomoto, A. C., James Howell, C., Hermes, D. J. and Katz, D. M. (2016). Mechanisms of Functional Hypoconnectivity in the Medial Prefrontal Cortex of Mecp2 Null Mice. *Cereb. Cortex* **26**, 1938–1956.

Schorge, S. and Colquhoun, D. (2003). Studies of NMDA receptor function and stoichiometry with truncated and tandem subunits. *J. Neurosci.* **23**, 1151–8.

Schutt, J., Falley, K., Richter, D., Kreienkamp, H.-J. and Kindler, S. (2009). Fragile X mental retardation protein regulates the levels of scaffold proteins and glutamate receptors in postsynaptic densities. *J. Biol. Chem.* **284**, 25479–25487.

Sepulveda, F. J., Bustos, F. J., Inostroza, E., Zúñiga, F. A., Neve, R. L., Montecino, M. and van Zundert, B. (2010). Differential roles of NMDA Receptor Subtypes NR2A and NR2B in dendritic branch development and requirement of RasGRF1. *J. Neurophysiol.* **103**, 1758–70.

She, K., Ferreira, J. S., Carvalho, A. L. and Craig, A. M. (2012). Glutamate binding to the GluN2B subunit controls surface trafficking of N-methyl-D-aspartate (NMDA) receptors. *J. Biol. Chem.* **287**, 27432–27445.

Stefanovic, S., DeMarco, B. A., Underwood, A., Williams, K. R., Bassell, G. J. and Mihailescu, M. R. (2015). Fragile X mental retardation protein interactions with a G quadruplex structure in the 3'-untranslated region of NR2B mRNA. *Mol. Biosyst.* **11**, 3222–3230.

Steigerwald, F., Schulz, T. W., Schenker, L. T., Kennedy, M. B., Seeburg, P. H. and Kohr, G. (2000). C-Terminal truncation of NR2A subunits impairs synaptic but not extrasynaptic localization of NMDA receptors. *J. Neurosci.* **20**, 4573–4581.

Stephenson, J. R., Wang, X., Perfitt, T. L., Parrish, W. P., Shonesy, B. C., Marks, C. R., Mortlock, D. P., Nakagawa, T., Sutcliffe, J. S. and Colbran, R. J. (2017). A Novel Human CAMK2A Mutation Disrupts Dendritic Morphology and Synaptic Transmission, and Causes ASD-Related Behaviors. *J. Neurosci.* **37**, 2216–2233.

Stessman, H. A. F., Xiong, B., Coe, B. P., Wang, T., Hoekzema, K., Fenckova, M., Kvarnung, M., Gerdts, J., Trinh, S., Cosemans, N., et al. (2017). Targeted sequencing identifies 91 neurodevelopmental-disorder risk genes with autism and developmental-disability biases. *Nat. Genet.* **49**, 515–526.

Swanger, S. A., Chen, W., Wells, G., Burger, P. B., Tankovic, A., Bhattacharya, S., Strong, K. L., Hu, C., Kusumoto, H., Zhang, J., et al. (2016). Mechanistic Insight into NMDA Receptor Dysregulation by Rare Variants in the GluN2A and GluN2B Agonist Binding Domains. *Am. J. Hum. Genet.* **99**, 1261–1280.

Takasaki, Y., Koide, T., Wang, C., Kimura, H., Xing, J., Kushima, I., Ishizuka, K., Mori, D., Sekiguchi, M., Ikeda, M., et al. (2016). Mutation screening of GRIN2B in schizophrenia and autism spectrum disorder in a Japanese population. *Sci. Rep.* **6**, 33311.

Talkowski, M. E., Rosenfeld, J. A., Blumenthal, I., Pillalamarri, V., Chiang, C., Heilbut, A., Ernst, C., Hanscom, C., Rossin, E., Lindgren, A. M., et al. (2012). Sequencing chromosomal abnormalities reveals neurodevelopmental loci that confer risk across diagnostic boundaries. *Cell* **149**, 525–537.

Tarabeux, J., Kebir, O., Gauthier, J., Hamdan, F. F., Xiong, L., Piton, A., Spiegelman, D., Henrion, E., Millet, B., Fathalli, F., et al. (2011). Rare mutations in N-methyl-D-aspartate glutamate receptors in autism spectrum disorders and schizophrenia. *Transl. Psychiatry* **1**, e55.

Tavazoie, S. F., Alvarez, V. A., Ridenour, D. A., Kwiatkowski, D. J. and Sabatini, B. L. (2005). Regulation of neuronal morphology and function by the tumor suppressors Tsc1 and Tsc2. *Nat Neurosci* **8**, 1727–1734.

Toft, A. K. H., Lundbye, C. J. and Banke, T. G. (2016). Dysregulated NMDA-Receptor Signaling Inhibits Long-Term Depression in a Mouse Model of Fragile X Syndrome. *J. Neurosci.* **36**, 9817–9827.

Uzunova, G., Hollander, E. and Shepherd, J. (2014). The role of ionotropic glutamate receptors in childhood neurodevelopmental disorders: autism spectrum disorders and fragile x syndrome. *Curr. Neuropharmacol.* **12**, 71–98.

Varghese, M., Keshav, N., Jacot-Descombes, S., Warda, T., Wicinski, B., Dickstein, D. L., Harony-Nicolas, H., De Rubeis, S., Drapeau, E., Buxbaum, J. D., et al. (2017). Autism spectrum disorder: neuropathology and animal models. *Acta Neuropathol.* **134**, 537–566.

Vyklicky, V., Krausova, B., Cerny, J., Ladislav, M., Smejkalova, T., Kysilov, B., Korinek, M., Danacikova, S., Horak, M., Chodounska, H., et al. (2018). Surface Expression, Function, and Pharmacology of Disease-Associated Mutations in the Membrane Domain of the Human GluN2B Subunit. *Front. Mol. Neurosci.* **11**, 110.

Wang, C.-C., Held, R. G., Chang, S.-C., Yang, L., Delpire, E., Ghosh, A. and Hall, B. J. (2011). A Critical Role for GluN2B-Containing NMDA Receptors in Cortical Development and Function. *Neuron* **72**, 789–805.

Wang, W., Rein, B., Zhang, F., Tan, T., Zhong, P., Qin, L. and Yan, Z. (2018). Chemogenetic Activation of Prefrontal Cortex Rescues Synaptic and Behavioral Deficits in a Mouse Model of 16p11.2 Deletion Syndrome. *J. Neurosci.* **38**, 5939–5948.

Watanabe, M., Inoue, Y., Sakimura, K. and Mishina, M. (1992). Developmental changes in distribution of NMDA receptor channel subunit mRNAs. *Neuroreport* **3**, 1138–1140.

Yoo, H. J., Cho, I. H., Park, M., Yang, S. Y. and Kim, S. A. (2012). Family based association of GRIN2A and GRIN2B with Korean autism spectrum disorders. *Neurosci. Lett.* **512**, 89–93.

Zhou, C., Jensen, F. E. and Sucher, N. J. (2009). Altered development of glutamatergic synapses in layer V pyramidal neurons in NR3A knockout mice. *Mol Cell Neurosci* **42**, 419–426.

Figures

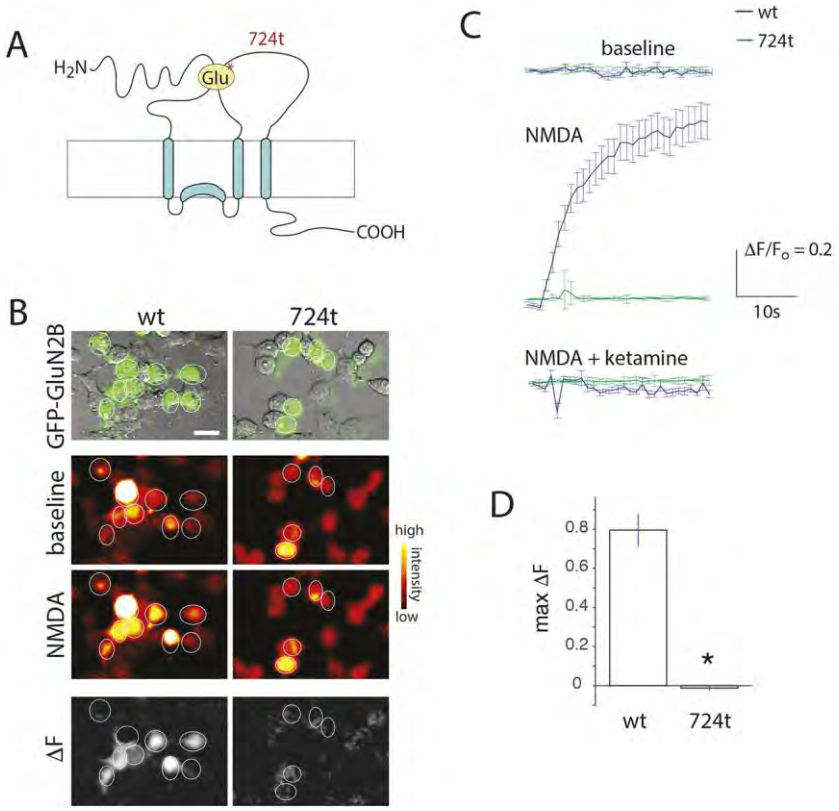

Figure 1. ASD-associated mutation in GluN2B abolishes calcium flux through NMDA receptors. **A.** Schematic of GluN2B illustrating the site of the ASD-associated mutation. The mutation (c.2172-2A>G) is predicted to produce a truncation at amino acid 724 (*724t*), eliminating the cytoplasmic tail, the fourth transmembrane domain, and a portion of the extracellular loop, which contributes to glutamate binding. **B.** Calcium influx is absent in cells expressing GluN2B^{724t}. HEK-293 cells were transfected with GluN1 and either GFP-GluN2B or GFP-GluN2B^{724t} then loaded with Fluo4-AM and imaged live. Images were collected at an initial, unstimulated *baseline* then stimulated with *NMDA*. The difference between baseline and stimulated fluorescence (*deltaF*) is shown in the *bottom panels*. Scale bar, 20µm. **C.** Quantification of Fluo4 calcium responses for wild-type GluN2B and GluN2B^{724t} reveals a consistent influx of calcium in response to NMDA stimulation (*NMDA*) for wild-type, but no response of the mutant receptors. The wild-type responses are due to NMDA

stimulation of NMDARs since calcium influx was absent in the presence of ketamine (*NMDA+ketamine*). Data are shown as the mean change in fluorescence normalized to the initial fluorescence ($deltaF/F_o$) with standard errors. **D**. Quantification of the maximal calcium influx for NMDARs containing $GluN2B^{WT}$ or $GluN2B^{724t}$. Mutant receptors did not display calcium influx, while wild-type receptors were functional (*, $p = 1.36 \times 10^{-10}$ (repeated measures ANOVA), n = 80 wild type cells and 40 mutant cells from 4 independent experiments). Data represent mean +/- S.E.

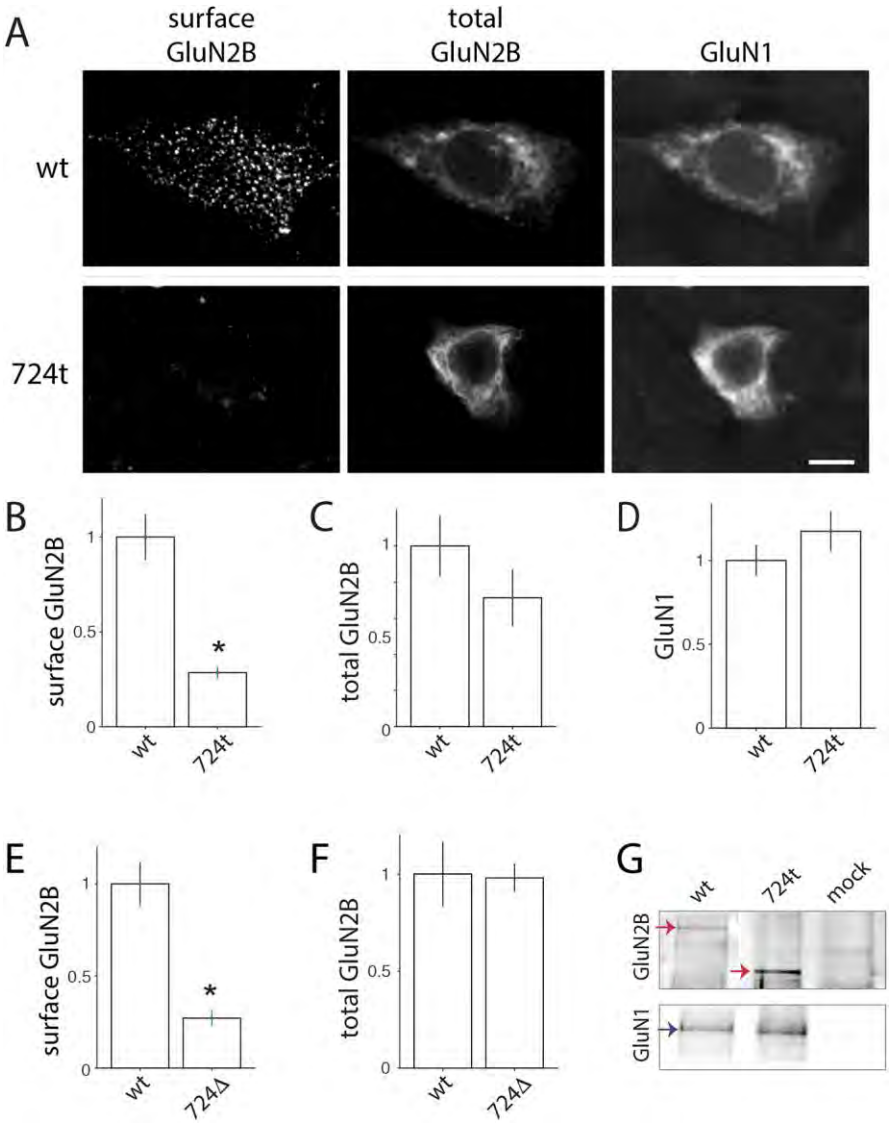

Figure 2. ASD-associated mutation in GluN2B prevents trafficking of NMDARs to the cell surface, without preventing co-assembly with GluN1. A. *Left panels,* Representative images of surface GFP-GluN2B in HEK-293 cells transfected with GluN1 and either GFP-GluN2B^{WT} (*top*) or GFP-GluN2B^{724t} (*bottom*). Labeling was performed in living unpermeabilized cells using anti-GFP antibodies. *Middle panels,* total GFP-GluN2B in the same cells. *Right panels,* GluN1-CFP in the same cells. CFP was fused to the intracellular domain of GluN1. Mutant GluN2B was not delivered to the plasma membrane. Lack of fluorescence at the surface was not due to reduced overall expression of GluN2B or GluN1. Scale bars, 10µm. **B.** Quantification of surface expression. Data represent mean +/- S.E. (*, p= < 0.0001, n = 64 GluN2B^{WT} cells and 41

GluN2B^{724t} cells from 4 independent experiments). **C-D.** Total GluN2B (C) and GluN1 (D) were equivalent in wild-type and 724t mutant neurons. **E-F.** Replacement of the final transmembrane domain and cytoplasmic tail was insufficient to restore trafficking of mutant NMDARs to the cell surface (*, p< 0.0001, n = 55 GluN2B^{WT} and 60 GluN2B$^{\Delta 724\text{-}786}$ neurons.) For (B-F), data represent mean +/- S.E. **G.** GluN2B^{724t} interacts with GluN1. HEK-293 cells were transfected with GluN1 and either wild-type GFP-GluN2B (*wt*) or GFP-GluN2B^{724t} (*724t*) then subjected to immunoprecipitation with anti-GFP antibodies. Immunoprecipitates were immunoblotted with antibodies that recognize GluN1 (*bottom*) and GluN2B (*top*). GluN1 co-immunoprecipitated with both wild-type and mutant GluN2B (*arrows*). The truncation mutation produced a smaller GluN2B protein. No signal was observed when immunoprecipitations were performed in the absence of GluN2B (*mock*). Statistical tests were ANOVA with Fisher's PLSD posthoc tests.

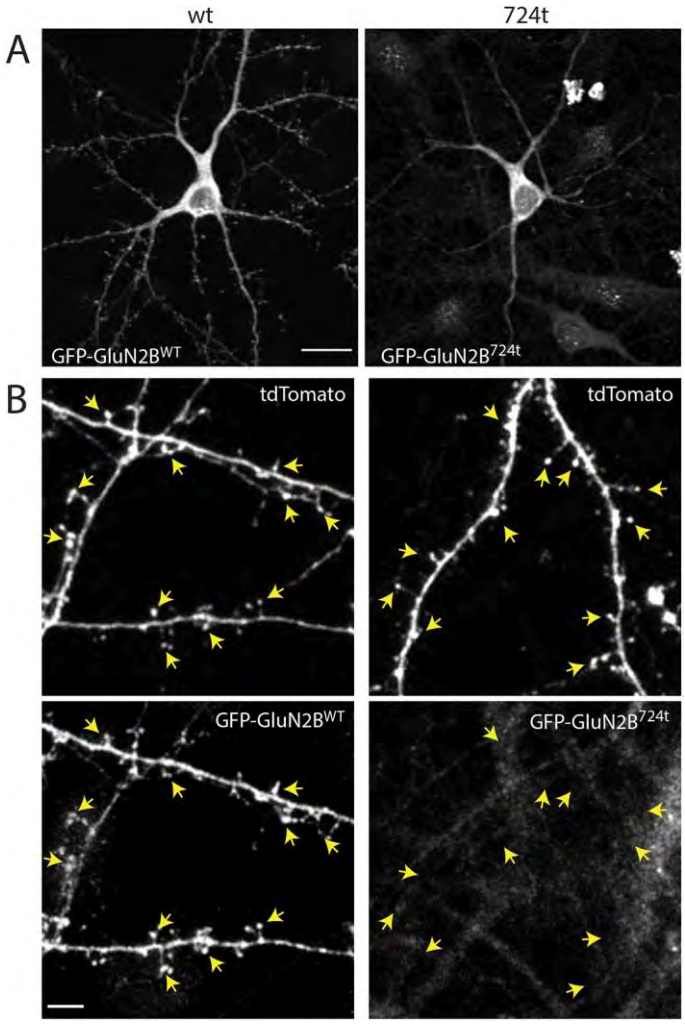

Figure 3. ASD mutation interferes with delivery of GluN2B to dendrites and dendritic spines. **A.** Representative images of neurons transfected with either GluN2B^{WT} (*left)* or GluN2B^{724t} (*right*). While GluN2B^{WT} appeared in numerous bright puncta throughout the dendrite arbor, GluN2B^{724t} was absent from dendrites or only dimly fluorescent within proximal dendrite shafts. When mutant subunits appeared in dendrites, the signal was diffuse rather than punctate. Scale bar, 20µm. **B.** Higher magnification images of dendritic spines of another set of neurons transfected with either GluN2B^{WT} (*left)* or GluN2B^{724t} (*right*). Neurons were co-transfected with tdTomato to fill neurons and visualize all spines (*top panels, arrows*). GluN2B^{724t} was not observed in dendritic spines, while GluN2B^{WT} was observed in most spines (*bottom*, *arrows*). Scale bar, 10µm.

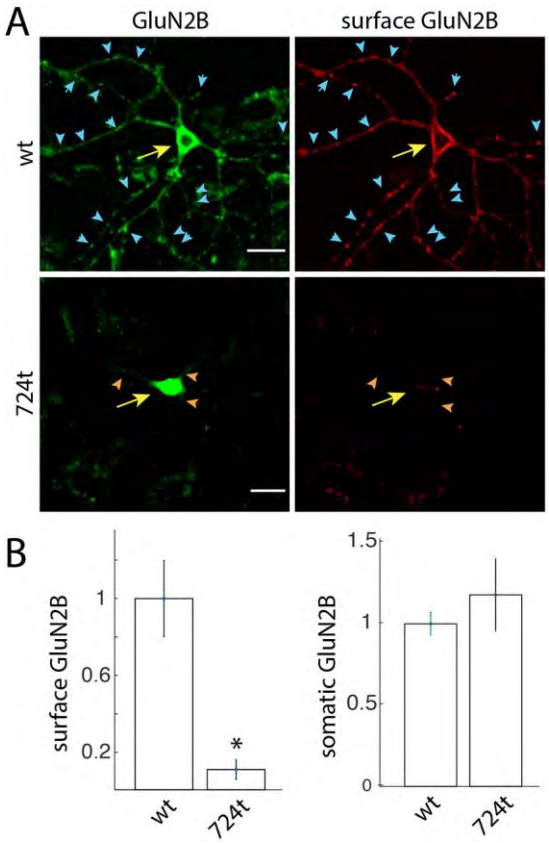

Figure 4. ASD-mutant GluN2B is not trafficked to the surface of neurons. A. Representative images of GluN2B (*green, left panels*) and surface GluN2B (*red, right panels*) in neurons expressing either GFP-GluN2B^{WT} or GFP-GluN2B^{724t}. In wild-type neurons, *arrowheads* indicate GluN2B puncta at the surface of dendrites. No GluN2B puncta were observed at the surface of mutant dendrites. *Arrows* indicate the location of the soma of the transfected neuron in each image. In the 724t images, *arrowheads* indicate the extent of GFP-GluN2B^{724t} spread within dendrites. Scale bars, 20 µm. **B.** Quantification of surface fluorescence in neurons expressing either GFP-GluN2B ^{WT} or GFP-GluN2B^{724t}. The ASD mutation prevented delivery to the cell surface (*, $p < 0.0001$, n = 13 GluN2B^{724t} and 14 GluN2B^{WT} neurons). **C.** Total somatic GluN2B expression was similar for GFP-GluN2B^{WT} and GFP-GluN2B^{724t}, indicating that the lack of surface localization was not due to reduced expression of GluN2B ($p = 0.4397$). Data represent mean +/- S.E. Statistical tests were ANOVA with Fisher's PLSD posthoc tests.

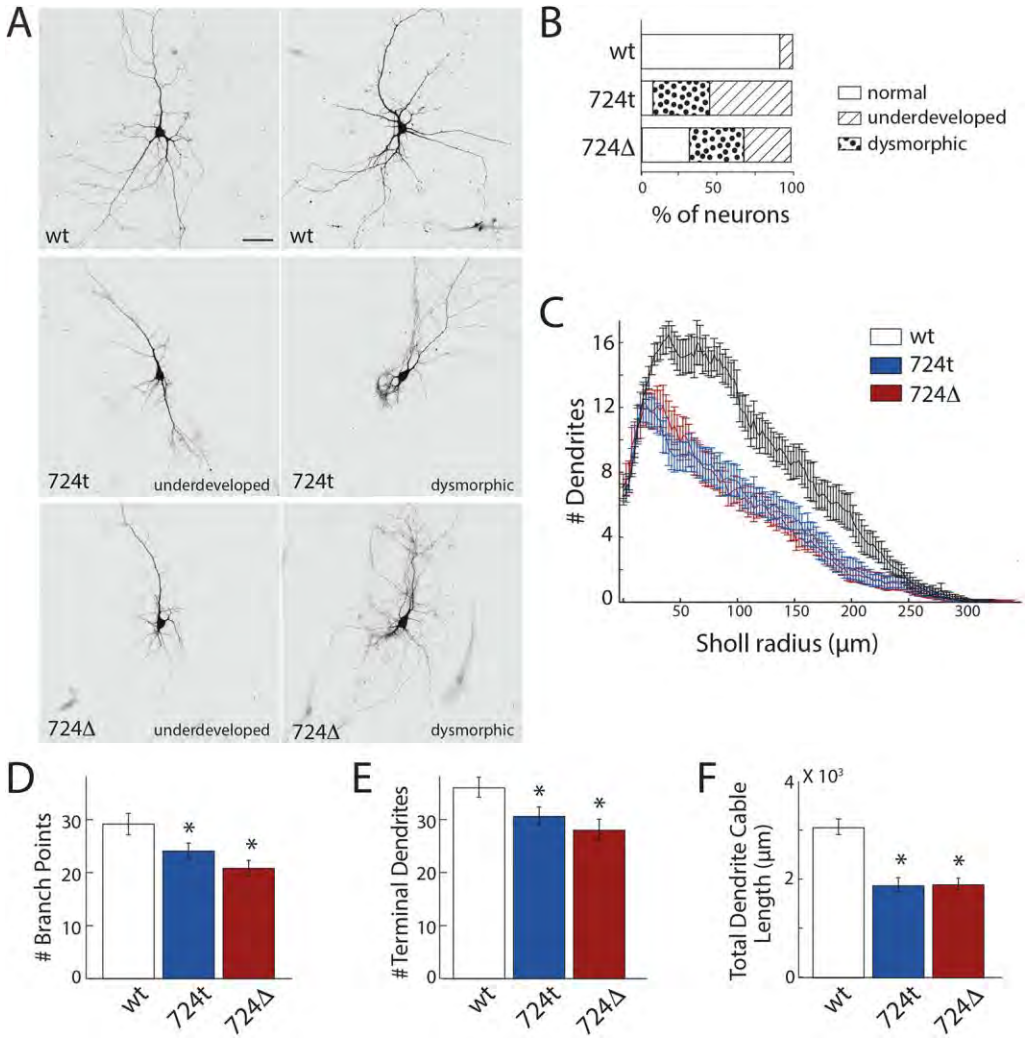

Figure 5. ASD-mutant GluN2B disrupts dendrite development. A. Representative images of neurons (14DIV) transfected with tdTomato, to fill the cells, and GFP-GluN2B^{WT} (*top row, wt*), GFP-GluN2B^{724t} (*middle row, 724t*), or GFP-GluN2B$^{\Delta 724\text{-}786}$ (*bottom row, 724Δ*). Scale bar, 20μm. Neurons that expressed mutant GluN2B displayed abnormal dendritic morphology. Some cells appeared to have dendrites that were under-developed (*left*), while others were highly dysmorphic (*right*). **B.** Prevalence of morphological types for neurons expressing wild-type GluN2B (*wt*), GluN2B^{724t} (*724t*) or GluN2B$^{\Delta 724\text{-}786}$ (*724Δ*). **C.** Sholl analysis of dendrites for neurons expressing wild-type or mutant GluN2B. **D-F.** Quantification of the mean number of branches (D, *, $p = 0.005$), number of terminal dendrites (E, *, $p = 0.0414$), and total dendrite cable length (F, *, $p < 0.0001$) for neurons expressing GluN2B^{WT} (*wt*), GluN2B^{724t} (*724t*)

or GluN2B$^{724\text{-}786}$ (*724*Δ). Data represent the mean +/- S.E. (n = 12 (wt), 15 (724t) and 15 (724Δ) neurons from multiple independent experiments). Statistical tests were ANOVA with Bonferroni corrections for multiple comparisons.

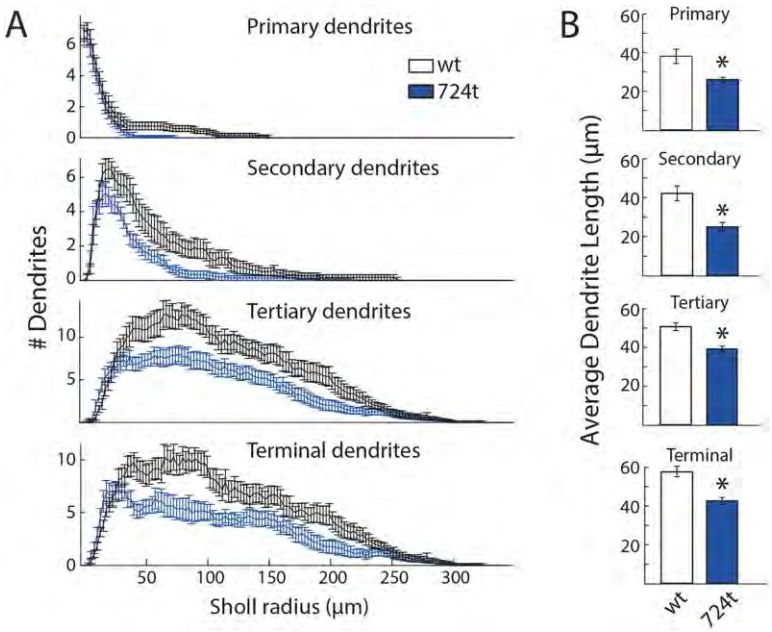

Figure 6. ASD-associated mutation in GluN2B reduces the number and length of intermediate and terminal dendrite segments. **A.** Sholl plots, separated by dendrite branch order. **B.** Mean length of dendrite segments, separated by branch order. Dendrite segment length was significantly reduced for all orders measured: primary (*, $p = 0.0014$), secondary (*, $p = 8.5 \times 10^{-5}$), tertiary or greater (*, $p = 4.16 \times 10^{-6}$) dendrites. Data represent the mean +/- S.E. (n = 12 (wt) and 15 (724t) neurons). Statistical tests were ANOVA with Bonferroni corrections for multiple comparisons.

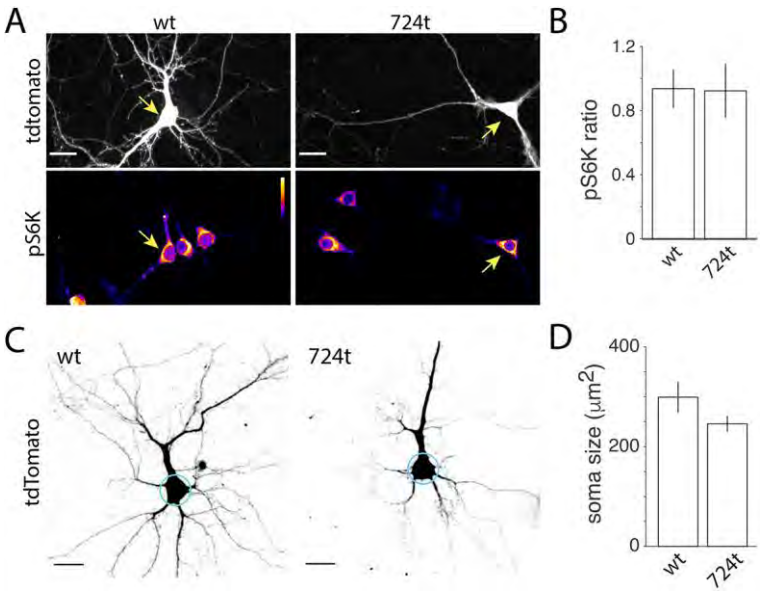

Figure 7. ASD-mutant GluN2B does not alter mTOR signaling or reduce soma size. A. Representative images showing fluorescence of pS6K in 11-14 day old neurons, as a measure of mTOR activity (*bottom panels*). Neurons transfected with either GFP-GluN2B^{WT} (*wt*) or GFP-GluN2B^{724t} (*724t*) co-expressed tdTomato to fill cells (*top panels*). Scale bars, 20μm. **B.** No discernible differences were observed in the mean intensities of pS6K within the somas of neurons expressing GluN2B^{WT} or GluN2B^{724t}. Data are presented as the ratio of pS6K in transfected neurons versus pS6K in neighboring untransfected neurons ($p = 0.955$, n = 8 GluN2B^{WT} neurons compared to 21 untransfected neighbors and 14 GluN2B^{724t} neurons compared to 40 untransfected neighbors). **C-D.** Reduced mTOR activation typically results in smaller soma size. Neurons expressing mutant GluN2B showed no significant shrinkage in soma area. Cortical neurons were transfected with either GluN2B^{WT} or GluN2B^{724t}, along with tdTomato to fill the cells. Somas were traced (C, *circles*) and quantified (D, $p = 0.1162$; n = 13 WT and 15 724t neurons from 3 experiments). Statistical tests were ANOVA with Fisher's PLSD posthoc tests.

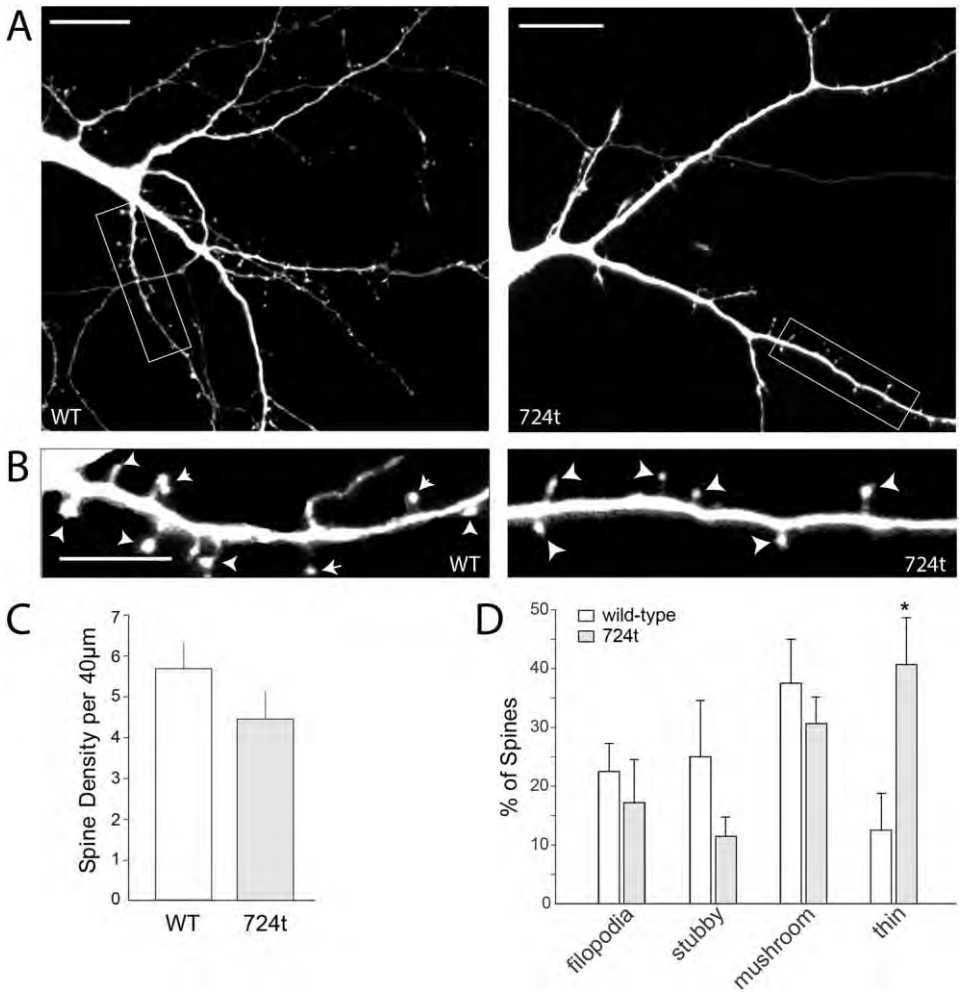

Figure 8. ASD-associated mutation in GluN2B did not affect spine density or morphology. **A**. Representative images of dendrites that were transfected with either GFP-GluN2B^{WT} (*left*) or GFP-GluN2B^{724t} (*right*) and co-transfected with a tdTomato fill. Scale bars, 20µm. **B**. Higher magnification views of the dendrite segments boxed in (A). *Left,* wild-type. *Right*, 724t. Spines are indicated by *white arrows*. Scale bar, 10µm. **C**. Dendritic spine densities were not significantly different between GFP-GluN2B^{WT} and GFP-GluN2B^{724t} neurons (p = 0.27, one-way ANOVA, n = 7 and 15 neurons for wild-type and mutant, respectively). **D.** Dendritic spine morphologies were similar for GFP-GluN2B^{WT} neurons and GFP-GluN2B^{724t} neurons. No significant change was observed for filopodia (p = 0.6076), stubby (p = 0.1546) and mushroom (p = 0.4272) spines, while thin spines were increased upon expression of the mutant (p = 0.0354), all by ANOVA (n = 39 wild-type and 64 mutant spines).

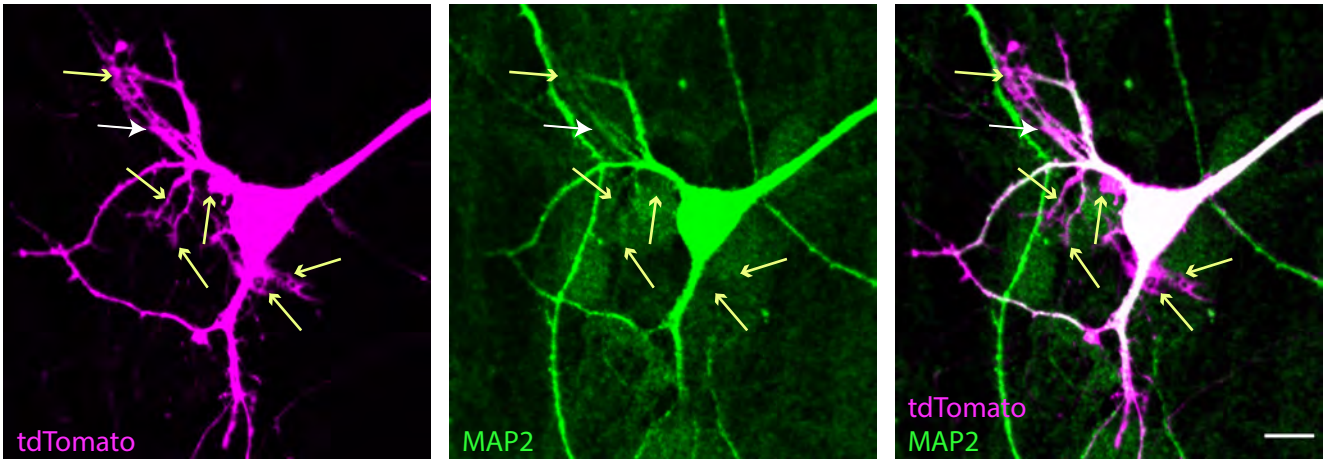

Figure S1. Abnormal structures of dysmorphic GluN2B^{724t} neurons only partially contain MAP2. Representative images of abnormal structures emanating from the soma and proximal dendrites of a dysmorphic neuron that expresses GFP-GluN2B^{724t}. Neurons were cotransfected with tdTomato (magenta) and immunolabeled with antibodies to MAP2 (green), a dendrite-specific marker. Co-localization of tdTomato and MAP2 is indicated by white in the overlay (right panel). This example of a dysmorphic neuron had a hairy mass emanating from its upper left side and additional abnormal structures protruding from the soma. The base of the hairy mass expressed some MAP2 (white arrow), while the distal portions of these structures and other filopodial and lamellipodial-like protrusions did not express MAP2 (yellow arrows). Longer, thick structures that resembled short dendrites did express MAP2. MAP2-positive dendrites that do not express tdTomato are from neighboring untransfected neurons. Scale bar, 10μm.

Journal of Cell Science • Supplementary information

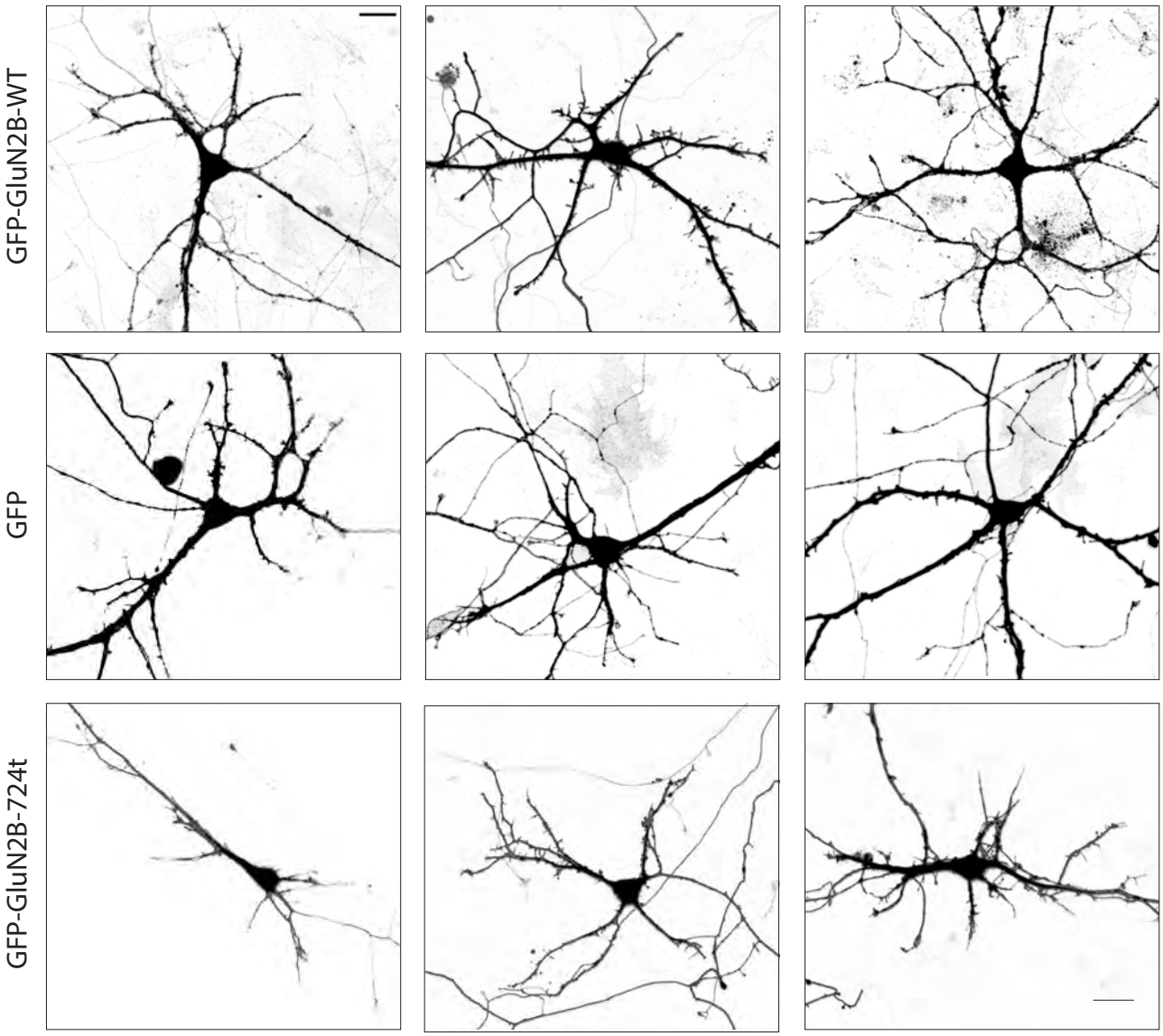

Figure S2. Examples of dendrites of neurons transfected with GFP alone, GFP-GluN2B^{WT} or GFP-GluN2B^{724t}. Each row comprises three examples for neurons transfected with the construct indicated on the left. tdTomato fills are shown to allow visualization of the full extent of the dendritic arbors. Neurons transfected with GFP-GluN2B^{724t} tended to appear underdeveloped or dysmorphic when compared to either GFP-GluN2B^{WT} or GFP-expressing neurons. In contrast, neurons transfected with either GFP or GFP-GluN2B ^{WT} generally appeared well-developed. Scale bars, 20µm

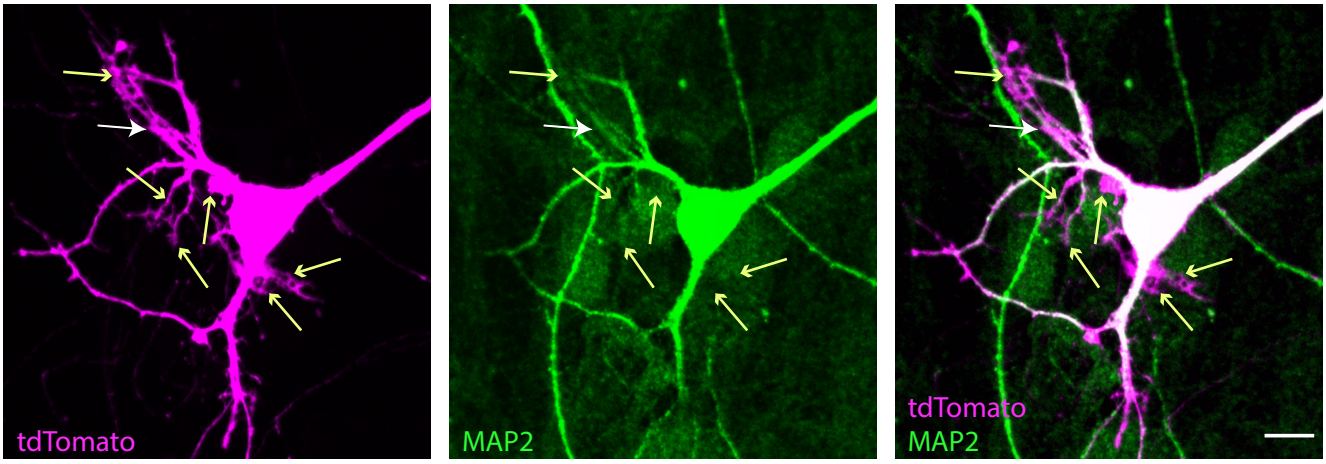

Figure S1. Abnormal structures of dysmorphic GluN2B^{724t} neurons only partially contain MAP2. Representative images of abnormal structures emanating from the soma and proximal dendrites of a dysmorphic neuron that expresses GFP-GluN2B^{724t}. Neurons were cotransfected with tdTomato (magenta) and immunolabeled with antibodies to MAP2 (green), a dendrite-specific marker. Co-localization of tdTomato and MAP2 is indicated by white in the overlay (right panel). This example of a dysmorphic neuron had a hairy mass emanating from its upper left side and additional abnormal structures protruding from the soma. The base of the hairy mass expressed some MAP2 (white arrow), while the distal portions of these structures and other filopodial and lamellipodial-like protrusions did not express MAP2 (yellow arrows). Longer, thick structures that resembled short dendrites did express MAP2. MAP2-positive dendrites that do not express tdTomato are from neighboring untransfected neurons. Scale bar, 10μm.

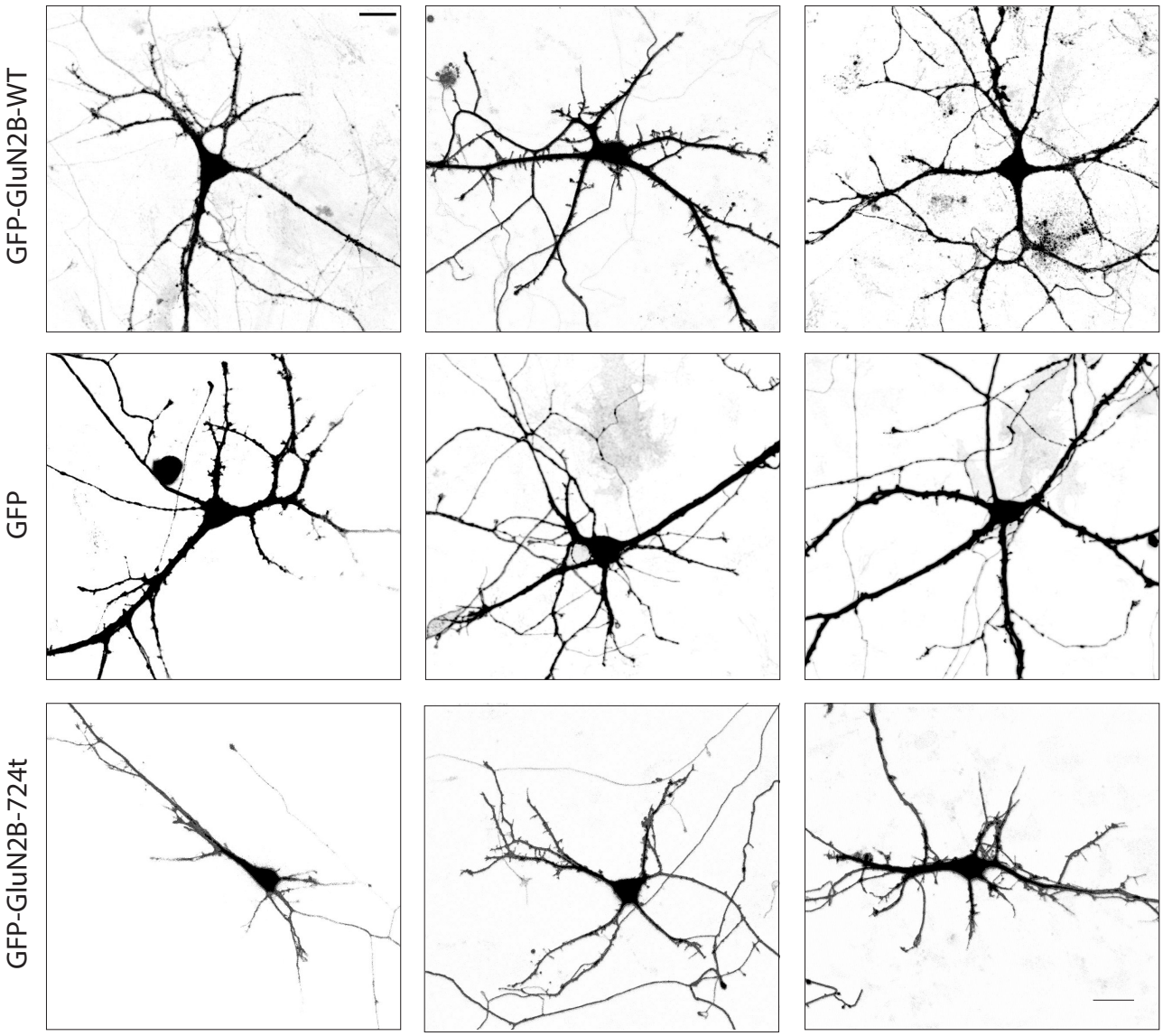

Figure S2. Examples of dendrites of neurons transfected with GFP alone, GFP-GluN2B^{WT} or GFP-GluN2B^{724t}. Each row comprises three examples for neurons transfected with the construct indicated on the left. tdTomato fills are shown to allow visualization of the full extent of the dendritic arbors. Neurons transfected with GFP-GluN2B^{724t} tended to appear underdeveloped or dysmorphic when compared to either GFP-GluN2B^{WT} or GFP-expressing neurons. In contrast, neurons transfected with either GFP or GFP-GluN2B ^{WT} generally appeared well-developed. Scale bars, 20µm